Available online at www.sciencedirect.com
ScienceDirect
Journal of Computational Physics 227 (2008) 5582–5609
JOURNAL OF COMPUTATIONAL PHYSICS
www.elsevier.com/locate/jcp

Full f gyrokinetic method for particle simulation of tokamak transport

J.A. Heikkinen [a,*], S.J. Janhunen [b], T.P. Kiviniemi [b], F. Ogando [b,c]

[a] Euratom-Tekes Association, VTT, P.O. Box 1000, FI-02044 VTT, Finland
[b] Euratom-Tekes Association, Helsinki University of Technology, P.O. Box 4100, FI-02015 TKK, Finland
[c] Universidad Nacional de Educación a Distancia, Madrid, Spain

Received 20 February 2007; received in revised form 21 December 2007; accepted 5 February 2008
Available online 23 February 2008

Abstract

A gyrokinetic particle-in-cell approach with direct implicit construction of the coefficient matrix of the Poisson equation from ion polarization and electron parallel nonlinearity is described and applied in global electrostatic toroidal plasma transport simulations. The method is applicable for calculation of the evolution of particle distribution function f including as special cases strong plasma pressure profile evolution by transport and formation of neoclassical flows. This is made feasible by full f formulation and by recording the charge density changes due to the ion polarization drift and electron acceleration along the local magnetic field while particles are advanced. The code has been validated against the linear predictions of the unstable ion temperature gradient mode growth rates and frequencies. Convergence and saturation in both turbulent and neoclassical limit of the ion heat conductivity is obtained with numerical noise well suppressed by a sufficiently large number of simulation particles. A first global full f validation of the neoclassical radial electric field in the presence of turbulence for a heated collisional tokamak plasma is obtained. At high Mach number ($M_p \sim 1$) of the poloidal flow, the radial electric field is significantly enhanced over the standard neoclassical prediction. The neoclassical radial electric field together with the related GAM oscillations is found to regulate the turbulent heat and particle diffusion levels particularly strongly in a large aspect ratio tokamak at low plasma current.

MSC: 65C20; 68U20; 76F10

Keywords: Particle simulation; Plasma; Turbulence

1. Introduction

Large-scale kinetic simulations of toroidal plasma dynamics based on first principles are called for in investigations on such transient transport mechanisms like Low (L) to High (H) confinement transport barrier formation or Edge Localized Modes (ELM) at the edge plasma, Internal Transport Barrier (ITB) formation in

* Corresponding author. Tel.: +358 20 722 5090; fax: +358 20 722 6390.
E-mail address: jukka.heikkinen@vtt.fi (J.A. Heikkinen).

0021-9991/$ - see front matter © 2008 Elsevier Inc. All rights reserved.
doi:10.1016/j.jcp.2008.02.013

the core plasma, or intermittent turbulence in magnetic fusion devices. Because of rapid or strong restructuring in the particle distribution function $f(\mathbf{x}, \mathbf{v}, t)$ and in the EM field, often contemporary with such transients, full f kinetic calculation is a necessity in such cases. First full f guiding-center particle simulation of the evolution and equilibrium of the neoclassical flows was presented in [1–3], where the method of one-dimensional ion polarization equation to solve for the flux-surface averaged radial electric field was introduced. In the forementioned works, the role of neoclassical mechanisms in the L–H transition was investigated and the effect of edge boundary and steepness of density and temperature profile on the magnitude of the radial electric field was evaluated. To obtain a complete picture of the transport barrier formation, one needs to incorporate turbulence into such a full f guiding-center simulation by inclusion of a three-dimensional (3D) solver for the EM field.

Following early full f electrostatic particle-in-cell simulations of turbulence in tori [4–6], which at that time were mostly done with an unrealistic electron–ion mass ratio and for a single toroidal mode number at a time, gyrokinetic (GK) model for averaged ion motion was developed [7] to eliminate the costly computing effort in following the particle Larmor orbits. By an examination of ion density response to a varying electrostatic field, the system of guiding center equations involving no polarization drift and having a modified (3D) Poisson equation which expresses an explicit response of ions to velocity phase fluctuations and first-order modification of magnetic moment were constructed and used to evolve the particle coordinates and field. In [8], the formalism in [7] has been developed to an energy-conserving set of gyrokinetic equations with Hamiltonian structure and to include electromagnetic fluctuations. Beyond the standard GK ordering, this set may allow [9] fluctuation frequencies of the order of ion gyrofrequency and for long wavelengths even perturbation amplitudes bringing the $\mathbf{E} \times \mathbf{B}$ drift of the order of ion thermal velocity. Although not yet universally proven, it is generally believed that the energy-conserving set with gyrokinetic ordering can be used for studies of long-time evolution of f far from its initial state. Here the problem, in particular in the presence of turbulence, is whether the high order nonlinearities neglected in the gyrokinetic ordering may in the very long time evolution contribute with noticeable effects. Also, the role of higher order gyrokinetic terms in evaluating the gyroviscosity effects on the neoclassical equilibrium has not yet been fully resolved [10]. In the following, these problems are not considered and the evolution of f is studied within the standard low order gyrokinetic terms.

After full f particle simulation tests [11] of the method in [7], the numerical implementation of GK method was further strengthened by a so called delta f technique [12], where only perturbed quantities are represented by simulation variables. With the delta f approach, GK plasma simulation for toroidal magnetic fusion devices has since then become a standard tool for turbulent transport analysis under conditions of weak perturbations (mostly in the core plasma) [12–21]. Fluid, Vlasov and particle approaches are used, the latter two being advantaged by a more precise kinetic description. Due to the need of full f kinetic simulations, a number of such gyrokinetic Vlasov and particle-in-cell codes based on the formalism in [8] have recently been developed [22–26]. A particular problem in the numerical implementation of gyrokinetic full f calculation is in the treatment of nonlinearities. Among others, this involves the way how to sample implicitly the integrated ion charge density response to velocity phase fluctuations and first-order modification of magnetic moment and how to sample the electron charge density response to acceleration parallel to ambient magnetic field by the electric field (electron parallel nonlinearity). In other words, the question arises how to consistently construct the coefficient matrix for the GK Poisson or Ampère equation with evolution of f. Here, a complicated integral of a differential operator on the product of f and the field potential is incorporated. In all previous works, this problem has been circumvented by taking a given fixed Maxwellian $f = f_0$ in the construction of the coefficient matrix for the GK Poisson equation. This is naturally the right procedure in delta f approach where only small deviations from the initial f_0 are considered, but for the full f simulation such a procedure is not acceptable.

Various techniques for dealing with the kinetic and non-adiabatic electrons in gyrokinetic particle codes have been developed [27–30] and have been applied in many of the previously mentioned codes. Common to these methods are approximations where part of the distribution function (usually untrapped electrons) is treated either analytically (adiabatic model) or in fluid moment expansion. With these methods, also the well-known problems [29] in resolving the electron current contribution to the right-hand side of the Ampère equation have been to a large extent solved. In Eulerian delta f continuum codes like GYRO, GS2, and GENE [15,16,32] the remedy is to ensure a term-by-term cancellation of the large terms in the electron current,

normally accomplished by unifying the discretization scheme for the different terms. These continuum codes have become particularly powerful in the studies of electrostatic and electromagnetic turbulence in experiments. However, the full f treatment of the electron parallel nonlinearity has not been addressed in delta f codes.

Recently, Eulerian full f methods to solve the gyrokinetic Vlasov equation have been introduced for the turbulence problem by inclusion of the polarization drift in the characteristics of the Vlasov equation and by using an unmodified Poisson equation to solve for the fields [33]. With this method using adiabatic electrons, although still in slab geometry, the complication in updating the coefficient matrix in the Poisson equation is naturally avoided. By explicit inclusion of the polarization drift in the gyrocentre motion, important effects have been demonstrated for very steep gradients in plasma pressure, as for the tokamak edge plasma [34,35]. Stimulated by Manfredi [33] Sosenko et al. [36] introduced appropriate GK equations for nonlinear perturbations within the standard GK approximations using an asymptotic theory of charged particle motion in an electrostatic field based on Krylov–Boholiubov averaging method. Here, it was found that the Poisson equation does not remain unmodified when polarization drift is included explicitly in the gyrocentre motion. In spite of this caveat, this model seems to provide an attractive technique for the treatment of the nonlinearity in the ion polarization and in full f realization of simulations.

In the present work, we will follow the work in [36] and describe an implicit computational GK particle solution method for the full f electrostatic plasma quasineutrality. The ion density change by polarization drift and electron density change by the parallel electron acceleration are sampled directly from the particle gyrocentre motion in terms of the unknown electrostatic potential at each time step. Being thus consistently full f, the present nonlinear particle method should provide a useful approach for such global and dynamic transport phenomena where strong restructuring in the particle distribution function $f(\mathbf{x}, \mathbf{v}, t)$ and in the EM field take place. As the ion polarization drift is included in the ion orbit motion, and is not treated in an integrated fashion separately from other drifts, the present approach allows nonlinear interaction of the polarization drift with other drifts present. The adopted technique for the implicit treatment of the charge density perturbation by ion polarization and electron parallel nonlinearity is based on the direct implicit time integration method of the particle acceleration in the electrostatic field developed earlier for unmagnetized plasmas [37].

A full f nonlinear 5D (two velocity and three configuration space coordinates) gyrokinetic particle-in-cell code ELMFIRE implementing the GK method in [36] and involving direct implicit treatment of the ion polarization and electron parallel nonlinearity is here described elaborately. The formulation and the equations to be solved with adopted orderings are introduced in Section 2. The algorithms for the implicit methods are explained in Section 3. Other important features of the code and an analysis of the noise ensuing from the finite number of simulation particles is presented in Section 4. This Section discusses the initialization for the finite ion orbits in a tokamak configuration, particle tracking, sampling and interpolation methods, binary collision method, boundary conditions and replacement of lost particles at boundaries, the adopted magnetic background as well as the overall performance of the code. The convergence issues and the validation of the code with respect to linear growth and frequency of the ion temperature gradient mode instabilities and benchmarks against turbulence saturation and neoclassical effects (where proper treatment of kinetic electrons is important) are given in Section 5. The developed code is applied for a global transport analysis in an FT-2 tokamak plasma (Fisichiskii Tokamak-2, Ioffe Institute, St Petersburg) [38] having lower hybrid (LH) ion heating. The transport coefficients and electrostatic field together with the density and temperature profiles are solved for the heated plasma and a qualitative comparison with some representative experimental data is presented in Section 6.

2. Nonlinear gyrokinetic equations in toroidal geometry

The gyrokinetic Vlasov–Poisson equations (with the collision term $C(\langle f \rangle)$) solved by the present method and based on the theory in [36] using the guiding-centre transformation $\mathbf{x} = \mathbf{R} + \mathbf{b} \times (\mathbf{v}_\perp - \mathrm{d}\mathbf{R}/\mathrm{d}t)/\Omega$ in an inhomogeneous plasma are

$$\frac{\partial \langle f \rangle}{\partial t} + \frac{\mathrm{d}v_\parallel}{\mathrm{d}t}\frac{\partial \langle f \rangle}{\partial v_\parallel} + \frac{\mathrm{d}\mathbf{R}}{\mathrm{d}t} \cdot \frac{\partial \langle f \rangle}{\partial \mathbf{R}} = C(\langle f \rangle) \tag{1}$$

$$\frac{q^2}{mB\varepsilon_0}\int\left\{(\Phi-\langle\Phi\rangle)\frac{\partial\langle f_i\rangle}{\partial\mu}+\frac{m}{q\Omega}[-\nabla\cdot(\langle f_i\rangle\nabla_\perp\langle\Phi\rangle)\right.$$
$$\left.+\nabla\cdot\int^{\phi}(\Phi-\langle\Phi\rangle)\,\mathrm{d}\phi\mathbf{b}\times\nabla\langle f_i\rangle]\right\}\mathrm{d}\mathbf{v}=-\frac{1}{\varepsilon_0}(q\bar{n}_i(\mathbf{x})-en_e(\mathbf{x})). \tag{2}$$

Here, $\Phi(\mathbf{x})$ is the electrostatic potential at the position $\mathbf{x}$, $\langle f\rangle(\mathbf{R},\mu,v_\parallel)=(2\pi)^{-1}\int f(\mathbf{x},\mathbf{v})\delta(\mathbf{x}-\mathbf{R}-\boldsymbol{\rho})\mathrm{d}\mathbf{x}\,\mathrm{d}\alpha$ is the distribution function of ion guiding centers, $\mu=v_\perp^2/2B$ is the lowest order adiabatic invariant (i.e., magnetic moment), $\mathrm{d}\mathbf{v}=(B/2\pi)\delta(\mathbf{R}+\boldsymbol{\rho}-\mathbf{x})\mathrm{d}\mathbf{R}\,\mathrm{d}\mu\,\mathrm{d}v_\parallel d\phi$ denotes the velocity phase space differential, q, m are the ion charge and the mass, respectively, and $\mathbf{B}=B\mathbf{b}$ is the magnetic field with the unit vector $\mathbf{b}$. The gyroaverage over the ion Larmor rotation is denoted by $\langle..\rangle$, which for the potential is given by $\langle\Phi\rangle(\mathbf{R},\mu)=(2\pi)^{-1}\int\Phi(\mathbf{x})\delta(\mathbf{x}-\mathbf{R}-\boldsymbol{\rho})\mathrm{d}\mathbf{x}\,\mathrm{d}\alpha$. In evaluating the gyroaverage, an approximative relation $\mathbf{x}=\mathbf{R}+\boldsymbol{\rho}$ compatible with the GK ordering is adopted with $\mathbf{R}$ denoting the position of the guiding-center and $\boldsymbol{\rho}=\mathbf{b}\times\mathbf{v}_\perp/\Omega$ is the ion Larmor radius and Ω the ion Larmor frequency. The variables $v_\parallel$ and $\mathbf{v}_\perp$ denote the ion parallel and perpendicular velocity components, respectively. The velocity differential $\mathrm{d}\mathbf{v}$ is defined keeping fixed $\mathbf{x}$, i.e., the phase angle ϕ runs around $\mathbf{x}$. On the other hand, in the gyroaverages the phase angle α runs around the guiding-center $\mathbf{R}$.

The GK formalism was derived within the standard GK ordering, i.e., $\omega/\Omega\sim\rho/L\sim E_\perp/Bv_\perp\sim\epsilon\ll 1$, where ω denotes the characteristic angular frequency of the perturbation, L describes the scale length of gradients in unperturbed distribution and background magnetic field, and $E_\perp$ is the magnitude of the perpendicular component (with respect to the magnetic field) of the electric field perturbation. The ion density $\bar{n}_i(\mathbf{x})=\int\langle f\rangle(\mathbf{R},\mu,v_\parallel)\mathrm{d}\mathbf{v}$ is obtained from the gyro-orbit around the ion guiding-center coordinates that are advanced with the polarization drift included. f_i denotes the ion distribution function and $n_\mathrm{e}(\mathbf{x})$ is the electron density at $\mathbf{x}$ as obtained within the drift-kinetic approximation from the guiding-center positions of the electrons. e is the elementary charge and ε_0 is the vacuum permittivity. The Laplacian $\nabla^2\Phi$ term has been neglected in the gyrokinetic Poisson equation. Summation over all ion species is implied in Eq. (2).

The equations for the gyrocentre motion of all particle species are given by

$$\frac{\mathrm{d}\mathbf{R}}{\mathrm{d}t}=v_\parallel\mathbf{b}+\frac{1}{B^*}\mathbf{b}\times\left[\frac{m\mu}{q}\nabla B+\frac{mv_\parallel^2}{q}\mathbf{b}\cdot\nabla\mathbf{b}+\nabla\Psi\right]-\frac{1}{\Omega B}\frac{\mathrm{d}\nabla\langle\Phi\rangle}{\mathrm{d}t} \tag{3}$$

$$m\frac{\mathrm{d}v_\parallel}{\mathrm{d}t}=-\left(\mathbf{b}+\frac{mv_\parallel}{qB^*}\mathbf{b}\times\mathbf{b}\cdot\nabla\mathbf{b}\right)\cdot(m\mu\nabla B+q\nabla\Psi), \tag{4}$$

where the renormalized potential is given by

$$\Psi=\langle\Phi\rangle-(q/2mB)\sum_{n\neq 0}\left[\frac{\partial|\Phi_n|^2}{\partial\mu}+\frac{iB}{n\Omega^2}\nabla\Phi_n\times\nabla\Phi_n^\star\cdot\hat{\mathbf{b}}\right], \tag{5}$$

where $\Phi_n=(1/2\pi)\int\mathrm{d}\alpha e^{in\alpha}\Phi(\mathbf{R},\mu,\alpha)$ ($\langle\Phi\rangle=\Phi_0$) with n in the sum running all integers except 0, and denotation with i for an imaginary number and ☆ for complex conjugate have been adopted. The nonlinear terms introduce the ponderomotive effects for large field perturbations, but their effects are not considered in the present work. Note that in obtaining the ion polarization drift, the potential is evaluated from $\langle\Phi\rangle$. For electrons, a drift-kinetic approximation is adopted which is obtained by the replacement $\langle\Phi\rangle=\Phi(\mathbf{R})$. The polarization drift is neglected for electrons. $\mathbf{B}^*=B^*\mathbf{b}+(mv_\parallel/q)\mathbf{b}\times\mathbf{b}\cdot\nabla\mathbf{b}$ with $B^*=B+(mv_\parallel/q)\mathbf{b}\cdot\nabla\times\mathbf{b}$ arise from the well-known Morozov–Soloviev [39] form of the guiding-centre motion. This second-order parallel drift correction is introduced strictly to preserve the Hamiltonian character of motion. Correspondingly, $\mathrm{d}\mathbf{v}=(B^*/2\pi)\delta(\mathbf{R}+\boldsymbol{\rho}-\mathbf{x})\mathrm{d}\mathbf{R}\,\mathrm{d}\mu\,\mathrm{d}v_\parallel\mathrm{d}\phi$.

Eqs. (1)–(5), agree with the standard gyrokinetic equations [8] in the electrostatic limit except for the explicit introduction of the polarization drift into the present gyrocentre equations of motion (the last term on the right hand side of the Eq. (3)) and for the appearance of the second term on the left-hand side of the gyrokinetic Poisson equation (2). The original equations based on Krylov–Boholiubov averaging were derived in [36] for a homogeneous plasma, and it was shown there that the introduction of the guiding-centre transformation $\mathbf{x}=\mathbf{R}+\mathbf{b}\times(\mathbf{v}_\perp-\mathrm{d}\mathbf{R}/\mathrm{d}t)/\Omega$ brings the second term on the left-hand side of Eq. (2) and adds the polarization

drift into the standard gyrokinetic equations given in [8]. After some straightforward but tedious algebra, one can show [40] that these same modifications apply also in the case of an inhomogeneous plasma so that Eqs. (1)–(5) result in such a case for the transformation $\mathbf{x} = \mathbf{R} + \mathbf{b} \times (\mathbf{v}_\perp - \mathbf{R}/\mathrm{d}t)/\Omega$. On the other hand, using the transformation $\mathbf{x} = \mathbf{R} + \mathbf{b} \times \mathbf{v}_\perp/\Omega$ the standard equations were reproduced in [36] with this new averaging technique. Also the canonical structure was constructed in the case of both transformations. Note that the Hamiltonian correction is not accounted for the polarization drift terms as these are higher order in the gyrokinetic ordering than the other drifts.

3. Direct implicit method for ion polarization and electron parallel nonlinearity

Before proceeding in presenting the overall (Section 3.1) structure of the numerical code, it is described how the direct implicit integration method [37] is applied in constructing the charge density responses to ion polarization drift and magnetic moment tremblings and to the electron acceleration along the magnetic field.

3.1. Ion polarization

In order to solve Eq. (2), one must either fix (or guess) the average ion distribution $\langle f \rangle$ and its gradients inside the integrals on the left hand side of equations, or construct the integrals directly from the full f particle simulation together with the solution of the gyrokinetic equation for the potential Φ. The latter method was first time used in [41] for the gyrokinetic Poisson equation given in [7], while in other gyrokinetic works using the standard equations, $\langle f \rangle$ has been fixed (usually a Maxwellian distribution has been used as a guess). The problem in direct implicit numerical construction of $\int \ldots \partial\langle f \rangle/\partial\mu \mathrm{d}\mathbf{v}$ is that this expression can not be transformed without severe complications to the form $\int \ldots \langle f \rangle \mathrm{d}\mathbf{v}$. The latter form is required for direct sampling of the integral from particle coordinate data.

In Eq. (2), in contrast to the standard gyrokinetic Poisson equation, the velocity phase space integral on the left-hand side is of higher order in $\kappa^2 = (k_\perp \rho)^2$. Here, $k_\perp$ characterizes the wavenumber in the perturbation modes perpendicular to the magnetic field. Partly due to this κ dependence, the integral has not dominant role in determination of the saturated state of turbulence or mode spectrum. Thus, one may here resort to a less accurate integration method where one constructs $\partial\langle f \rangle/\partial\mu$ (and similar spatial derivatives of $\langle f \rangle$) separately from Φ by statistically collecting the particle coordinate information inside appropriate regions around $\mathbf{x}$. The distribution function and its gradients collected statistically in this way for the phase space grid cells can then be used for approximation of the integrals and the coefficient matrix of the Poisson equation. With a reasonable amount of simulation particles or grid cells, this method is statistically too inaccurate to be used for the corresponding integral in the standard gyrokinetic Poisson equation, where the integral has a dominant role in turbulence saturation.

In order to avoid complications in solving Eq. (2) arising from the smallness of its left hand side, the perturbation in ion density $\bar{n}_i(\mathbf{x})$ by the ion polarization drift velocity $\mathbf{v}_\mathrm{p} = (1/\Omega B)\mathrm{d}\langle \mathbf{E} \rangle/\mathrm{d}t$ is also calculated during simulation. This direct calculation is made implicit in $\mathbf{E}$ by evaluating the change in the ion polarization density $\delta\bar{n}_{pk}$ at a cell j by the k'th ion polarization shift $\mathrm{d}\mathbf{s} = (1/\Omega B)(\langle \mathbf{E} \rangle - \langle \mathbf{E}^m \rangle)$ during the time step $\mathrm{d}t$ as

$$\delta\bar{n}_{pk}(j) = \frac{1}{\Omega B \mathrm{d}V_j} \sum_\mathrm{i} \sum_\mathrm{p} \sum_l w_\mathrm{i}[f_{xij} a_l \Phi_{pl} + f_{yij} b_l \Phi_{pl}] - \frac{1}{\Omega B \mathrm{d}V_j} \sum_\mathrm{i} [\langle E_x^m \rangle f_{xij}^m + \langle E_y^m \rangle f_{yij}^m], \tag{6}$$

where the gyroaveraged electric field $\langle \mathbf{E} \rangle = \sum_\mathrm{p} \sum_l (a_l \Phi_{pl} \hat{\mathbf{x}} + b_l \Phi_{pl} \hat{\mathbf{y}})$ has been interpolated from the potential grid values Φ_{pl} around each point $x_\mathrm{p}, y_\mathrm{p}$ on the Larmor circle of the k'th ion, with interpolation coefficients a_l and b_l involving also the differential operator on Φ to obtain the electric field, and summed over these points to obtain the Larmor average. w_i is the weight of the i'th subparticle on the Larmor circle of the particle k. We have $\mathrm{d}\mathbf{s} = \mathrm{d}x\hat{\mathbf{x}} + \mathrm{d}y\hat{\mathbf{y}}$ for the polarization shift of the k'th ion perpendicular to the magnetic field with $\hat{\mathbf{x}}$ and $\hat{\mathbf{y}}$ denoting the unit vectors on the polarization plane. The particle cloud fraction derivatives $f_{xij} = \mathrm{d}f_{ij}/\mathrm{d}x$ and $f_{yij} = \mathrm{d}f_{ij}/\mathrm{d}y$ for the shift of the i'th subparticle cloud in each direction are obtained from the fraction f_{ij} of the cloud of the i'th particle within the cell j. $\mathrm{d}V_j$ is the volume of the j'th cell. The quantities with the upper index m are the values at the start of the time step. Thus, in Eq. (6) $\mathbf{E}^m$ is the electric field at the start of the time step

dt, and $\mathbf{E}$ is that (unknown) at the end of the time step. For the charge density on the right hand side of Eq. (2), $q\bar{n}_i(\mathbf{x}) - en_e(\mathbf{x})$, one obtains after summing Eq. (6) over all particles k an expression $q\sum_k \delta\bar{n}_{pk}(j) + q\sum_k\sum_i w_{ki}f_{kij}/\mathrm{d}V_j - e\sum_k w_{ke}f_{kej}/\mathrm{d}V_j$, where $\sum_k\sum_i w_{ki}f_{kij}/\mathrm{d}V_j$ denotes the ion density obtained in the cell j at the end of the time step dt from the guiding-center motion but without the polarization drift arising during the step dt. $\sum_k w_{ke}f_{kej}/\mathrm{d}V_j$ is the electron density at the end of the time step obtained within the drift-kinetic approximation. Finite Larmor radius effects are neglected for electrons so that no subparticles or polarization drift are applied for them. Introducing the expression of charge density into Eq. (2), one may evaluate the potential $\Phi(\mathbf{x})$ at each grid point after the time step dt. $\langle E_x\rangle$ and $\langle E_y\rangle$ are stored for each particle after each time step from the resolved Φ, and are thus available as $\langle E_x^m\rangle$ and $\langle E_y^m\rangle$ at the next time step. In contrast to other methods, here the ions are advanced according to polarization drift keeping the sampled f consistent with particle motion. The polarization drift of each ion is calculated at the end of the time step dt from $\mathrm{d}\mathbf{s} = (1/\Omega B)(\langle\mathbf{E}\rangle - \langle\mathbf{E}^m\rangle)$ using the evaluated field $\mathbf{E}$, and is added to the ion coordinates. Thus, at the start of any time step, the ion coordinates represent the full solution of the guiding-center equations including the polarization drift.

Although formally similar to the standard GK method where an analytically (and from other drifts separately) calculated cumulative sum of the ion response over the whole history of the particle motion $q\tilde{n}_{pi}$ is separated from the charge density of the Poisson equation, the present technique numerically calculates and separates only the change of $q\delta\bar{n}_{pi}$ arising during each time step.

The present technique increases somewhat the CPU and memory requirements in comparison to the method with a fixed $\langle f\rangle$ and analytically evaluated $\tilde{n}_{pi}(\mathbf{x})$, but with a nine point interpolation for the field and using four subparticle points on each ion Larmor radius, only 20% increase in CPU requirement has been recorded over that with the standard gyrokinetic equation (with the given $\langle f\rangle$). With a similar implicit solver for the electron density perturbation by the parallel electric field acceleration, good stability properties of the algorithm have been observed making possible to use time steps beyond the standard semi-implicit limit [31].

3.2. Implicit kinetic electrons

In fully kinetic electron simulations, electron dynamics determine the shortest time step increasing the CPU usage significantly when compared to simulations with adiabatic electrons. An accurate electron time step is less than $\Delta t \leqslant \Delta z/v_T$ with grid cell size $\Delta z = 2\pi R/N_z$ in magnetic field direction where R is the major radius of the tokamak and v_T is the electron thermal velocity. For $R = 0.5$ m, $N_z = 4$ and $T_0 = 400$ eV, one has $\Delta t = 10^{-7}$ s. To ensure stability with the time step Δt reaching the accuracy limit, the electron parallel motion is treated implicitly [37]. Electron density $n_e(t_n)$ at each global time step t_n can be sampled from locations $\mathbf{x}_k(t_n)$ of each particle. Electron density at next step $n_e(t_{n+1})$ can be evaluated from the sum of sampled densities $\tilde{n}_e + \delta n_e$, where $\tilde{n}_e$ is sampled from the electron positions $\tilde{\mathbf{x}}$ obtained at time t_{n+1} ensuing from the guiding-center motion from t_n till $t_{n+1} = t_n + \Delta t$, but excluding here the electron motion arising from the parallel acceleration due to $\nabla_\parallel\Phi$: $\Delta v_\parallel = e\nabla_\parallel\Phi\Delta t/m_e$, $\Delta z = e\nabla_\parallel\Phi\Delta t^2/2m_e$ (here, we have neglected the electromagnetic curvature effects in the electron motion obtained from Eq. (4)). The fully implicit effect of $\mathbf{E}_\parallel$ on $\mathbf{x}_k(t_{n+1})$ is obtained in terms of $\tilde{\mathbf{x}}(t_{n+1})$ and the unknown $\Phi(t_{n+1})$ using the adopted force interpolation as

$$\delta\mathbf{x}_k = -(e\Delta t^2/2m_e)\sum_\ell c_\ell\Phi_\ell(t_{n+1})\hat{z},$$

where the z-component of the electric field $\mathbf{E}_z = \sum_\ell c_\ell\Phi_\ell\hat{z}$ acting on the k'th electron is interpolated from the potential grid values Φ_ℓ around each point $\tilde{\mathbf{x}}_k$ with interpolation coefficients c_ℓ involving also the differential operation on Φ to obtain the electric field. To construct the derivatives of Φ, we used both two-point as well as three-point approximation for the derivative. The two-point approximation was found to be accurate enough for the present scheme. Now, the density modification $\delta n_{ek}(j)$ at a cell j by the k'th electron's parallel shift $\delta\mathbf{x}_k$ is

$$\delta n_{ek}(j) = -(e\Delta t^2/2m_e)(1/\mathrm{d}V_j)\sum_\ell w_k f_{zkj}c_\ell\Phi_\ell(t_{n+1}), \tag{7}$$

where w_k is the weight of the k'th electron. The particle cloud fraction derivative f_{xkj} for the shift of the electron cloud in the z-direction is made from the fraction f_{kj} of the cloud of the k'th electron within the cell j. Sampling

over all particles k constructs explicitly the total density change $\delta n_e(j)$ at the cell j. We have then $n_e = \tilde{n}_e + \delta n_e$ at t_{n+1} and $\mathbf{x}_k(t_{n+1}) = \tilde{\mathbf{x}}_k(t_{n+1}) + \delta\mathbf{x}_k$ for each particle k. Since δn_e is constructed in a matrix form $\mathbf{A}\cdot\Phi$, it can be moved to the left hand side of Eq. (2) from the right hand side and the final equation reads as

$$-\frac{q}{\varepsilon_0}\mathbf{A}\cdot\Phi+\frac{q}{\varepsilon_0}\delta\bar{n}_{pi}+(q^2/mB\epsilon_0)\int\left\{(\Phi-\langle\Phi\rangle)\frac{\partial\langle f_i\rangle}{\partial\mu}+\frac{m}{q\Omega}[-\nabla\cdot(\langle f_i\rangle\nabla_\perp\langle\Phi\rangle)\right.$$
$$\left.+\nabla\cdot\int^{\phi}(\Phi-\langle\Phi\rangle)\mathrm{d}\phi\mathbf{b}\times\nabla\langle f_i\rangle]\right\}\mathrm{d}\mathbf{v}=-\frac{q}{\varepsilon_0}[\tilde{n}_i(t_{n+1})-\tilde{n}_e] \tag{8}$$

which can be solved implicitly.

An implicit technique for electrons has been previously [31] used only in an approximate fashion based on a guessed f with $\mathbf{A}\cdot\Phi\approx 0.5\omega_{pe}^2\Delta t^2\nabla_\parallel^2\Phi$, but including also semi-implicit variations of it. The present sampled, fully implicit technique was successfully benchmarked against this approximation in conditions where the approximation is expected to be good.

4. Methods for a global full f code

4.1. General remarks

Various gyrokinetic particle codes for 5D toroidal configuration have been developed, and many features in them are shared by the present approach. However, the latter differs from them not only in the full f feature and in the choice of the GK equations. The majority of other GK codes have been written for adiabatic electrons. Alternatively, in simulations with kinetic electrons [27–30,42] flux tube domain or special consideration for trapped electron group (in the magnetic well) have been applied making possible only local or approximative calculations. In the present work, the whole electron distribution is solved implicitly within the drift-kinetic approximation. Various heat source models and multiple ion species for impurity with the loop voltage provide the possibility to study the plasma pressure and momentum profiles evolution to equilibrium in global transport simulations. This is further controlled by a recycling model of outflowing particles from the outer boundary. The collisions among all particles are evaluated with the binary collision model introduced in [43]. The collision operator is approximated in the drift-kinetic limit, i.e., finite Larmor radius effects are not considered in the operator. Thus, no classical diffusion across $\mathbf{B}$ is modelled. The electrostatic field is solved directly in a 3D grid of quasi-ballooning coordinates [44] without any Fourier solver. The particle initialization on invariant phase space accounting for pre-evaluated finite ion orbits, as first introduced in [2], is adopted. The asymptotic motion of gyrocentres is implemented on Boozer coordinates [45]. Here, the standard gyrokinetic equations are incremented with the ion polarization drift as described in [36]. In the following, some of these features of the full f gyrokinetic formalism are described in more details for their numerical implementation.

4.2. Orbit following and sampling

In numerical implementation of Eq. (2), its right-hand side and the coefficient matrix for Φ in a given mesh constructed for $\mathbf{x}$ are calculated at each time step by sampling from the positions and weights of the simulation particles, ions and electrons, obtained by advancing the gyrocentres of the particles according to Eqs. (3) and (4) with a fourth-order Runge–Kutta scheme. The polarization density as given in Eq. (6) and the electron parallel nonlinearity density in Eq. (7) are sampled at the same time as the corresponding density obtained without polarization drift and without parallel electron acceleration at that time step. $\sum_k q\delta\bar{n}_{pk}$ and δn_{ek} are then added to the left-hand side of Eq. (2) before inversion of this equation for $\Phi(\mathbf{x})$. After the inversion, the remaining gyrocentre motion by ion polarization drift and electron parallel acceleration is calculated and the coordinates of the particle gyrocentres are updated accordingly. One should note here that although the system (1)–(5) is here solved implicitly for the ion polarization drift and electron parallel nonlinearity, the solution method still remains explicit for the other drifts like $\mathbf{E}\times\mathbf{B}$ and magnetic drifts and for the parallel inertia.

Two different coordinate systems are used in the code to get an optimal accuracy and resolution. Orbits are followed in straight-field-line coordinates (ψ, θ, ζ) [45] and potential is solved in quasi-ballooning coordinates (ψ, χ, ζ) [44]. Here, ψ is radial coordinate, ζ is toroidal coordinate and relation between the two poloidal coordinates is $\chi = \theta - \widehat{\iota}(\psi)\zeta$ with $\widehat{\iota}(\psi) \simeq \iota(\psi) = 1/q_s(\psi)$. Here, q_s is safety factor. Two coordinate systems are used to avoid poor resolution in solving potential structures in straight-field-line coordinates and problems with periodicity condition in ballooning coordinates. Grid is needed only in quasi-ballooning coordinates where the potential is solved and sampling is performed. Typically, in all three coordinates, the grid cells are equidistant but option of non-equidistant grid exists in $\psi - \chi$ directions.

In sampling the coefficients of Φ and densities $\tilde{n}_\mathrm{i}$ and n_e at $\mathbf{x}$ from the particle guiding-center positions $\mathbf{R} = \mathbf{x} - \boldsymbol{\rho}$, nearest grid-point (NGP), cloud-in-cell (CIC), and subtracted dipole (SD) schemes have been tested and CIC technique [46] was chosen for sampling. Also, for interpolation in calculating the force on particles from the potential the same technique is used. The magnetic background is specified in White-Chance straight-field-line coordinates (ψ, θ, ζ) [45] taking $B = B_0 R_0/R$ for the magnetic field B dependence on the major radius R. The quantities with the zero index are taken at the magnetic axis. In the benchmark tests and simulations to be discussed in Sections 5 and 6, we assume magnetic surfaces with circular poloidal cross-section and with no Shafranov shift. The latter assumptions mean an order of r^2/R^2 error in specifying θ which is reflected in similar steady perturbation of poloidal distribution of particle density. This has been reduced to order r^3/R^3 by a modification of the relation of θ to the true poloidal angle.

No smoothing algorithm is applied except near the boundaries where flux surface average of charge density separation on the right-hand side of Eq. (2) is taken in 1–3 radial grid points next to the boundary before solving Eq. (2). This has a tendency to decrease perturbations at the edge. For the validation tests to be described appropriate Fourier filtering both for the charge separation and the potential has been adopted where necessary.

4.3. Initialization

In the toroidal plasma simulation, it is common to try to initialize the particles in such a way that after the first time step the sampling constructs given initial density and temperature profiles in radial, poloidal, and toroidal directions. However, for wide particle orbits and arbitrary collisionality in non-circular tokamak geometry this task is difficult. For weak collisionality, methods [47] based on variable transformation to constants-of-motion space have been used in various studies of finite orbit effects for both initialization and further calculations. Although not restricted to, initialization to the Maxwellian velocity distribution with the local temperature is performed and zero initial electrostatic potential is often assumed. If no such account for phase space effects would be taken, the resulting profiles of macroscopic variables could be far from the wanted profiles. Even more seriously, there can transiently exist a finite net radial current even with closed orbits and no collisions. This transient current decays away with oscillations on a few bounce time scales, but may severely perturb the solution for the $\mathbf{E}$ dynamics as noted in [2]. This can be avoided to a large extent by initializing particles in an invariant space that spans the different particle orbits.

An initialization of ions on numerically pre-evaluated collisionless orbits is adopted here to guarantee that no strong radial current arises at the start from the radial inhomogeneity even in the presence of collisions. Due to the finite collisionality, no attempt to create given density, temperature, and poloidal/toroidal flow distributions was made. The effect of turbulence which often sets on an ion bounce time scale would actually make any such trial impossible. Therefore, in the initialization we have called for a zero radial flux surface averaged particle flux after the first time step. This so called quiescent initialization was introduced in Ref. [2]. Starting coordinates in radius, poloidal and toroidal angles, velocity and velocity pitch are first selected for the particles in such a way that these after sampling at the start would construct the wished particle distribution function $f(\mathbf{x}, \mathbf{v})$. Using these coordinates as initial values, collisionless virtual orbits are pre-evaluated by numerically integrating the adopted gyrokinetic equations of motion (using constant time step δt for each such an integration) for each initialization. The varying coordinates on the orbit are saved as coordinate sets $(\mathbf{R}(t_\mathrm{i}), \mu(t_\mathrm{i}), v_\parallel(t_\mathrm{i}))$ in memory at every time step $t_\mathrm{i} = i\delta t$ used. After this, a set of particle coordinates to be used as initial values in the actual simulation is selected randomly among the saved coordinate sets on the virtual orbit. This random selection ensures

that the radial particle flux is statistically small at the start. Similar methods have been incorporated also in other codes [17,23].

After initialising ions on collisionless orbits, for each ion, one electron is initialized at the same location to ensure quasi-neutrality. This is done at the gyro-orbit of each ion since the ion densities and matrix coefficients are sampled from the gyro-orbit, not from the gyrocentre. However, one should note that collisions, turbulence, and neoclassical effects with poloidal non-uniformity in pressure make it very difficult to initialize the plasma in equilibrium without causing numerical transients. Therefore, strong restructuring of $f(\mathbf{x}, \mathbf{v}, t)$ at the start of simulation follows almost always in practice, even with this quiescent initialization. In the benchmark tests for the linear growth of the unstable modes, where the onset of oscillations in $\mathbf{E}$ by radial currents is not a problem, the quiescent initialization is not used but instead the starting coordinates used otherwise for the integration of virtual orbits are applied.

4.4. Boundary conditions

In poloidal and toroidal direction boundary conditions in straight-field-line coordinates are trivial and in quasi-ballooning coordinates they are explained in Ref. [44]. In radial direction, the computational effort is reduced enormously by restricting the simulation to a relevant region $r_L < r < r_R$. Whenever there are no special constraints at the boundaries r_L and r_R posed by the problem, and when the mass flow parallel to the magnetic field is given at the boundaries, $\mathbf{E}$ can be evaluated in the region $r_L < r < r_R$ by using the well-known neoclassical analytical ambipolar value $E_a(r)$ as the boundary condition at $r = r_L$ and $r = r_R$. However, in GK particle codes it has been found necessary to shield the boundaries by special buffer regions where the potential and/or the particle densities are made evanescent (see e.g. [16,48]). This means that in practice one applies $\Phi = 0$ conditions at the boundaries. In the present method, we have found it possible to apply a given radial electric field E_r boundary value (without setting $\Phi = 0$) at the other boundary (either at inner or the outer boundary) and a given Φ at the opposite boundary without any evanescent potential regions or suppression of particle weights. What has been important for the stability of boundaries has been the flux-surface averaging of the charge separation within the buffer regions (1–3 grid widths from the boundaries) around boundaries. What is important for a valid outer boundary condition in transport simulations is that no transport plug is created at the boundary by smoothing or averaging the field or charge separation. This is an important complication of the full f calculation, where the numerical stability of the boundaries is an issue.

In the following ideal benchmark tests and examples with no metallic boundaries, we have set $\Phi = 0$ at the inner boundary and $E_r = 0$ at the outer boundary. On boundaries in contact with metal, zero potential or sheath potential condition is applied. At the inner boundary, the outflowing particles are reflected. This is accomplished by following the orbits for $r < r_L$ in the absence of collisions and polarization drift, and stopping the clock during the time the particles spend in these regions. This is consistent with the assumption of no toroidal momentum source and zero radial current for $r < r_L$. At the outer boundary, the same method can be used and the particles hitting the divertor or wall outside $r > r_R$ can be treated in the same way as explained in Ref. [2] with prompt reinitialization at $r = r_R$ uniformly in pitch and poloidal angle, with the local Maxwellian velocity distribution.

In more realistic simulations, pairwise reinitialization of outflowing ions and electrons according to assumed neutral distribution or ionization on randomly directed straight return paths of recycled neutrals is chosen. This maintains the otherwise flattening density profile. In this method, each outflowing particle at each time step is registered. After the global time step is finished for the whole particle ensemble, the sum of the total charge $W_\mathrm{i} = \sum_a N_a Z_a e w_a$ of the lost ions is compared to that of electrons, $W_\mathrm{e} = N_\mathrm{e} e w_\mathrm{e}$. Here, a denotes the ion species, Z_a its charge number, N_a is the number of the lost particles in species a and w_a is the weight of this species. In the present code version, the weights for each ion species are determined from the condition $Z_a w_a = w_\mathrm{e}$, and equal weights are used among the particles within the same species. Hence, the pairwise reinitialization is performed up to the charge W_a or W_e, which one is smaller. The rest of the particles, i.e., the unpaired particles, are reinitialized at $r = r_R$. The paired particles, however, are reinitialised according to a model for neutral ionization deeper in the plasma as cold ion–electron pairs. As these pairs now have exactly zero total charge, no net charge is carried deeper into the plasma. At the outer edge, exactly the same charge remains as the net charge what was flowing through the outer edge.

In sampling, gyro-circles extending outside the calculation domain at the radial boundaries are reflected back to the domain. Otherwise total charge at the simulation regime would not conserve. To sample the ion polarization density from the gyro-radii extending outside the calculation domain, the boundary conditions of the electrostatic potential are used to treat both the reflected and original ion contributions. For the code stability at boundaries, a consistent consideration of sampling of both local density as well as the GK coefficient matrix elements from the outflowing particles at the boundaries was necessary. Here, the present method with Eq. (2) was found more stable than with the standard gyrokinetic Poisson equation.

4.5. Numerical noise and accuracy

The numerical noise created by a finite number of simulation particles makes global full f gyrokinetic simulations demanding as regards computing time and memory usage. In general, the noise level in the particle simulations reduces as $1/\sqrt{N}$, where N is the average number of simulation particles in each cell. The noise not only makes it difficult to isolate physical fluctuations of plasma density and electrostatic potential from the fluctuations ensuing from the finite number of simulation particles but also creates unphysical particle and heat flux and demolishes the neoclassical equilibrium. To quantify this effect consider the mixing-length estimate $\delta n/n = 1/k_\perp L_n$ for the nonlinear saturation level of physical fluctuations. Here, L_n is the density gradient scale length. In the case of Cyclone Base case linear benchmark to be discussed in the next Section, $k_\perp \rho_i$ in range 0.2–0.3 is found for the maximum growth of the unstable turbulent spectrum and $L_n/\rho_i = 500$. Here, the ion Larmor radius is denoted by ρ_i. Hence, $\delta n/n \sim 0.01$ is predicted for the rms fluctuation level of physical fluctuations. When $N \sim 1500$ in the simulation, the $1/\sqrt{N}$ noise is actually somewhat higher for density fluctuation level than expected for physical fluctuations in this case. In spite of this caveat, by appropriate filtering of data either in time or wavenumber, the linear growth rates of the unstable modes can be satisfactorily identified behind this noise. Clearly, the noise problem is enhanced by the choice of relatively low temperature and weak density gradient.

For steeper density gradient and higher temperature, the physical density fluctuations are much better resolved at saturation according to the mixing-length prediction. According to the adiabatic relation $e\Phi/T = \delta n/n$, these scalings are reflected in potential fluctuations, too, but the noise fluctuations of potential will increase linearly with plasma temperature, too. Although the charge density separation becomes by several orders of magnitudes smaller than either ion or electron density, the overall effect of adding ion and electron noise does not count more than to a twofold enhancement of potential fluctuation level after inversion of the Poisson equation. This is due to the fact that the quasineutrality is enforced to noise, too. Another twofold enhancement to potential fluctuations arises from the statistical sampling of the coefficient matrix of the GK Poisson equation from the ion and electron implicit terms in our present method.

To give a prediction for the contribution of the noise to ion heat conductivity (see, e.g. Fig. 4), consider noise potential fluctuations on a magnetic surface having τ as a decorrelation time for fluctuations. The radial diffusion coefficient can be estimated from $D = \langle \mathrm{d}r^2 \rangle / \tau$, where $\mathrm{d}r$ is the particle shift from the surface by the radial $E \times B$ velocity during the decorrelation time. Taking $\mathrm{d}r = \langle \Phi \rangle_{\mathrm{rms}} \tau / B \Delta y$, we find an estimate

$$D = \langle \Phi \rangle_{\mathrm{rms}}^2 \tau / B^2 \Delta y^2, \tag{9}$$

where Δy denotes the grid cell size in the poloidal direction. The decorrelation time can be estimated from $\tau = \Delta z / v_{Te}$, where Δz is the grid cell size along the magnetic field line. Here, the dominant noise is assumed to be created by electron free motion along the magnetic field, and is taken to be decorrelated by the time electrons can pass one cell element along the field line.

It is easy to see that the diffusivity by the noise according to our estimate scales as $T^{3/2}$ if an adiabatic potential response is assumed, while the mixing-length estimate of χ from the physical fluctuations similarly scales as $T^{3/2}$. Therefore, although helping us to identify the physical density fluctuations from noise, the increasing temperature does not help to resolve the physical ion heat conductivity if the number of simulation particles is too low. However higher temperature implies longer wavelengths for unstable modes and thus a coarser grid can be used in the simulation. This makes higher the number of particles per cell (N), and $\langle \Phi \rangle_{\mathrm{rms}}$ is reduced for that reason and also because of the longer Δy, which implies smaller noise flux.

However, one should note that both physical and noise radial fluxes of electrons and ions by $E \times B$ drift create net current due to the ion gyroaveraging [49]. This current density is proportional to $k_\perp^2 \rho_i^2 \Gamma_e/4$, where Γ_e is the radial particle flux of electrons. $k_\perp$ represents here the dominant part of fluctuations responsible for the flux. This non-ambipolarity is incorporated into the neoclassical equilibrium. Its most direct implication is that the radial electric field in the equilibrium becomes dependent on this non-ambipolar current. The latter is negative which makes the radial electric field more positive in equilibrium. Due to the noise contribution in the particle fluxes, the noise can deteriorate the accuracy in obtaining the radial electric field and flow velocities of the plasma. This is in particular the case where the radial noise flux of particles dominates over the corresponding flux of particles by physical fluctuations and over the ion flux by ion–ion collisions. The effect is further strengthened for the noise due to the dominant role the short wavelengths have in the noise potential spectrum in driving radial particle flux (implying larger $k_\perp^2 \rho_i^2$ in the non-ambipolar current formula).

The least constraints for the required number of simulation particles to suppress the noise can be found in applications where L_n is not too large and temperature not too small. Other parameters like L_T/L_n, characteristics of turbulent spectrum, or grid specifications may equally affect the required number of simulation particles. In the case of FT-2 tokamak plasma parameters in Table 2, a good statistics with little role of noise in transport quantities is obtained with $N > 800$. This is due to short $L_n = 0.08$ m and relatively high temperature of $T = 100$–500 eV. For practical applications, as will be shown in the following Sections, $N = 500$–5000 depending on the nonlinear saturation level of turbulence should be enough for sufficiently good statistics using the full f PIC method.

Time step in the kinetic simulation was found to be restricted by numerical electron heating [46] rather than the accuracy of the simulation even though the implicit solver for the electrons described in Section 3.2 has made possible to use time steps much beyond the standard semi-implicit limit [31]. The inertial streaming is treated explicitly, while the parallel acceleration is considered implicitly treating thus properly the stiffness arising from this term to the gyrokinetic equations. This mixture of explicit–implicit methods has however some limitations. The inertial streaming is firstly considered in calculations, before the parallel acceleration. That arises the question whether the electric field causing the acceleration is sampled at the correct position, since it could have altered considerably the streaming. This condition can be stated in the way that the method will be precise as long as the parallel shift due to the acceleration is much smaller than the inertial streaming, which in turn is limited in a time step by a Courant-like condition. The expression for both toroidal movements (Δz_s due to streaming and Δz_a due to acceleration) is the following

$$\Delta z_s = v_e \Delta t \approx \left[\frac{2k_B T_e}{m_e}\right]^{1/2} \Delta t,$$

$$\Delta z_a = \frac{e\partial_z \Phi}{2m_e} (\Delta t)^2,$$

$$\Delta z_a < \Delta z_s \rightarrow \Delta t < \left[\frac{8m_e k_B T_e}{e(\partial_z \Phi)^2}\right]^{1/2}.$$

This limitation for the time step is around 2 μs for the following unfavourable set of parameters: $T_e = 100$ eV, $\partial_z \Phi = 100/0.1 = 1000$ V/m (unrealistically high). The currently used time step is two orders of magnitude below the limit, ensuring the locality of the acceleration shift. Typical runs show consistently stable T_e regimes which are being perturbed only by externally posed heating or by the boundary zone of outward heat flux. The latter process is caused by the outer boundary conditions, which replaces outgoing particles with cold ion–electron pairs from neutrals. No numerical electron cooling has been found to arise from the present implicit treatment of the electron parallel nonlinearity.

While the accuracy in r and χ directions may be a problem especially at the outer edge, numerical accuracy from $\Delta t \leqslant \Delta z/v_{Te} \propto T_e^{-1/2} N_z^{-1}$ condition is most critical at the inner edge where the temperature is higher. Here, N_z is the number of grid cells in the toroidal direction. Thus, increase in the number of toroidal grid points in order to get better resolution increases CPU and memory requirements both because more particles are needed and, also, because one needs to shorten the time step. For the cases studied in the present work, an

upper time step limit of 5×10^{-8} s has been found to ensure a sufficient suppression of numerical heating ($\Delta t \leqslant \Delta z/v_{Te}$ condition giving $\tau = 10^{-7}$ s at inner edge and $\tau = 3 \times 10^{-7}$ s at the outer) for a reasonable N_z.

Other aspects that are of importance in convergence and resolution are for example how the contributions of the particles are sampled and derivatives are differentiated (see Section 3.1). A sufficient number of gyroaveraging points in typical runs was found to be four as the excited modes had $\kappa^2 < 1$. Increasing the number of gyroaveraging would not change the results remarkably here but would increase the CPU usage. For studies of the modes with $\kappa^2 \sim 1$, however this number has to be increased.

4.6. Computer memory considerations

Because of its high consumption of computational resources, the code has been successfully prepared and optimized for parallel execution on different multiprocessor platforms. It has been run both in IBM eServer 1600 and in different PC clusters. Inter-processor communication is held using the MPI standard for sake of efficiency and compatibility. Matrix inversion is performed by means of computational linear algebra packages. The use of IBM's PESSL and open source PETSc is implemented in the code for optimum performance depending on the platform used.

The heaviest memory demand and communication load take place during construction of the coefficient matrix of the GK equation of the electromagnetic field. Data collected from particles are stored in binary tree-like buffers (AVL) before being sent to the corresponding processors. This method minimizes the memory consumption and amount of data being transferred among processors [50].

Further reduce in communication times can be achieved by means of domain decomposition. The implementation of a system splitting into toroidal domains is under way. It will reduce the amount of data transfers between processors, which will reduce computation times specially in massively parallel computations.

5. Linear and nonlinear comparisons

A relatively large variety of gyrokinetic and gyrofluid simulation models for investigating microinstabilities and turbulence exist, and to build confidence in the results produced by these models, a rigorous benchmarking procedure for cross-validation must be adopted. In this section we present benchmarks of the code for the neoclassical behavior, for the linear mode instability regime with respect to a widely used test case, and to a case with kinetic electron physics and for nonlinear saturation level of heat diffusion. Also numerical convergence tests are presented. Here, the nonlinear terms in Eq. (5) have been neglected to ease the comparison with other codes where these terms are not included.

In the linear and nonlinear comparative tests we adopt the so-called "Cyclone DIII-D base case" dimensionless parameters [13] with hydrogen ions, a widely used test case described in Table 1. Correspondingly, initial density and temperature radial profiles are given as $n_0\left[1+\alpha_n \tanh\frac{r_0-r}{\alpha_n L_n}\right]$, $T_0\left[1+\alpha_T \tanh\frac{r_0-r}{\alpha_T L_T}\right]$ with $\alpha_n = \alpha_T = 0.95$, $r_0 = (r_L + r_R)/2$, $n_0 = 5 \cdot 10^{19}$ m^{-3}, $T_0 = 100$ eV, for the analysis of the Cyclone base case in the adiabatic case. In the kinetic electron case we use an initial density $n_0 = 5 \cdot 10^{17}$ m^{-3} and $\alpha_n = \alpha_T = 0.9$. For the linear analysis, the inner and outer radii of the simulation region are $r_L = 0.16$ m, $r_R = 0.024$ m with $a = 0.3975$ m as the minor radius. The plasma current density profile is taken as $j = j_0(1 - r^2/a^2)^{\alpha_J}$ with $j_0 = I_0(1+\alpha_J)/\pi a^2$ giving the maximum current density in terms of the total plasma current I_0 and minor radius a. In the following, we have $\alpha_J = 3.0$, $B_T = 1.1$ T, $R = 1.1$ m, and $I_0 = 200$ kA. At $r = r_0$, $\rho_i/a = 0.0023$.

For the transport simulations, we have chosen the FT-2 tokamak configuration described in Table 2. The toroidal magnetic field is $B = 2.2$ T and the total plasma current is $I_0 = 22$ kA, and initial density and temper-

Table 1
Initial parameters for the "cyclone base case" test cases with adiabatic and kinetic electrons

$R/L_T = 6.9$	$R/L_n = 2.2$	$R/a = 2.78$	$r_0/a = 0.5$	$q_s(r_0) = 1.43$	$\hat{s} = 0.78$
$T_i(r_0) = 100$ eV	$\Delta r/\rho_i = 2.87$	$r\Delta\theta/\rho_i = 4.19$	$\Delta\varphi = 0.393$		

The temperature and density scale lengths at $r = r_0$ are given by $L_T^{-1} = |\nabla \ln T|$ and $L_n^{-1} = |\nabla \ln n|$, respectively, R is the major radius and a is the minor radius, $\hat{s} = \frac{r}{q_s}\frac{dq_s}{dr}$ is the magnetic shear, and q_s is the magnetic safety factor,

Table 2
Initial parameters for the FT-2 transport simulations

$R/L_T = 8.3$	$R/L_n = 36.67$	$R/a = 6.875$	$r_0/a = 0.625$	$\hat{s} = 0.462$	$q_s(r_0) = 3.58$
$\Delta r/\rho_i = 2.84$	$r\Delta\theta/\rho_i = 2.23$	$\Delta\varphi = 1.57$			

The temperature and density scale lengths are given by $L_T^{-1} = |\nabla \ln T|$ and $L_n^{-1} = |\nabla \ln n|$, respectively, at $r_0 = 0.05$ m. R is the major radius and a is the minor radius, $\hat{s} = \frac{r}{q_s}\frac{dq_s}{dr}$ is the magnetic shear, and q_s is the magnetic safety factor.

ature radial profiles are given as $n_0[1-(r/a)^2]^{\alpha_n} + n_1$, $T_0[1-(r/a)^2]^{\alpha_T} + T_1$ with $\alpha_n = 2.5$ and $\alpha_T = 1.3$, $n_0 = 5\times10^{19}$ m^{-3}, and $n_1 = 1\times10^{18}$ m^{-3}. For electrons we have $T_0 = 350$ eV and $T_1 = 15$ eV and for the deuterium ions $T_0 = 180$ eV and $T_1 = 15$ eV. In simulations, we have $r_L = 0.021$ m, $r_R = 0.08$ m, with $a = 0.08$ m as the minor radius and $R = 0.55$ m as the major radius. The current density profile is parabolic with $\alpha_I = 1$. At $r/a = 0.5$, $\rho_i/a = 0.01$.

The electron model used in adiabatic simulations assumes Boltzmann-distributed electrons, whose response to an electric potential Φ is taken as

$$n_e = \langle n_i\rangle + \delta n_e = \langle n_i\rangle e^{\frac{e(\Phi-\langle\Phi\rangle)}{T_e}} \approx \langle n_i\rangle\left(1 + \frac{e(\Phi-\langle\Phi\rangle)}{T_e}\right), \tag{10}$$

where $\langle n_i\rangle$ and $\langle\Phi\rangle$ are the flux surface averages of the simulated ion density and potential. This model allows for the ion temperature gradient instability, but not any instabilities associated with electron motion such as trapped electron modes or electron temperature gradient modes.

5.1. Neo-classical benchmarking

In current advanced confinement regimes in tokamaks the ion heat flux is often observed to reduce locally to neoclassical levels. It is therefore important to have a simulation model which includes proper neoclassical flows in addition to turbulent transport. Here, we first quote the analytic equations and the results of previous particle simulations of neoclassical quantities in the absence of turbulence and, then, report the results of neoclassical tests done with the present gyrokinetic code.

5.1.1. Analytic equations

The non-ambipolar state terminates in a quasi-stationary state in which the 'ambipolar' E_r is determined by the toroidal angular momentum and the pressure gradient driven diamagnetic flows. An expression for this ambipolar E_r given in the literature is [51]

$$E_r = \frac{T_e}{e}\left(\frac{n_i'}{n_i} + \gamma\frac{T_i'}{T_i}\right) + B_p U_\parallel, \tag{11}$$

in which $U_\parallel$ is the average parallel flow velocity, B_p is the poloidal magnetic field component and T_i (T_e) the ion (electron) temperature, prime denotes the derivative with respect to radius, and γ is a coefficient depending on the normalized collisionality $\nu_{*i} = \nu_{ii}Rq_s/v_T\epsilon^{3/2}$ (expression which is valid in all collisionality regimes is given in Eq. (6.136) of Ref. [51]). Here, $v_T = (2T/m)^{1/2}$ is the thermal velocity, ϵ is the inverse aspect ratio and ν_{ii} is the ion–ion collision frequency. Using Eq. (6.131) of Ref. [51], expression for neoclassical heat diffusion coefficient reads as

$$\chi_{neo} = K_2\sqrt{\epsilon}\rho_p^2\nu_{ii}/\sqrt{2}, \tag{12}$$

where $\rho_p = v_T m/eB_p$ is the poloidal Larmor radius. The coefficient K_2 is given in [52], taking into account small inverse aspect ratio corrections, as

$$K_2 = 0.66\left(\frac{K_2^*/0.66}{1+1.03\sqrt{\nu_{*i}}+0.31\nu_{*i}} + \frac{1.77\nu_{*i}\epsilon^{3/2}}{1+0.74\nu_{*i}\epsilon^{3/2}}F\right), \tag{13}$$

where $F \approx \epsilon^{3/2}$ and $K_2^* = (0.66 + 1.88\sqrt{\epsilon} - 1.54\epsilon)(1+1.5\epsilon^2)$.

Previously, before developing the present gyrokinetic version of the code, the neoclassical behavior was investigated in the flux surface averaged potential approximation where the field is evaluated from the balance of flux surface averaged radial currents [2]. For (in time) fixed radial electric field E_r, the numerical model was tested in Refs. [53] by calculating poloidal rotation relaxation rates for a homogeneous plasma, and by comparing the perpendicular conductivity and parallel viscosity with the analytical estimates. The simulations were carried out for a wide range of collisionalities and rotation velocities. Quantitative agreement was found, but, of course, some differences exist which were traced to arise from various simplifications made in *analytic* theory. With non-fixed E_r, i.e., solving the electrostatic potential from the radial flux-surfaced current balance in the flux surface averaged potential approximation [2], E_r was found to approach and agree with the neoclassical analytical estimate [51] of the radial electric field in the wide parameter range, where the standard neoclassical theory is valid, including all the collisionality regimes. This comparison was made possible by investigations where the effect of boundaries on the evolution of the interior plasma region was carefully considered and controlled. In special regimes including either very steep density and temperature profiles [54] or super Mach poloidal flows [55], results in line with other more advanced neoclassical theories [56] were found.

5.1.2. Gyrokinetic simulation of neoclassical E_r and GAM:s

In the present gyrokinetic version of the code, flux-surface averaging the electrostatic potential obtained from Eq. (2) before calculation of the guiding-center motion has reproduced the neoclassical results obtained by solving the potential from the flux-surface averaged radial current balance described above. In the following, we wish to investigate the behavior of Φ for the complete solution of the guiding-center motion without any flux surface averaging. As a first neoclassical benchmark case we study the appearance of neoclassical equilibrium as a result of steadying after initial transients. The geodesic acoustic mode (GAM) oscillations are produced in the system by initializing a particle distribution function (e.g. based on a poloidally nearly homogeneous local Maxwellian velocity distribution), which is not a proper neoclassical equilibrium [57].

The time evolution of the radial profiles of the flux surface averaged potential and temperature and density are shown in Fig. 1 for the FT-2 configuration with kinetic electrons. Quiescent initialization is used which however is not able to suppress the radial current caused by improper distribution of particles at initialization (with respect to a neoclassical equilibrium). The configuration is given in Table 2. The plasma is heated by electron Ohmic heating (loop voltage of 0.5 V with an effective charge of $Z = 1$) and by 70–100 kW off-axis lower hybrid (LH) wave ion heating. The strength of the ion perpendicular velocity diffusion at the Landau resonance of the LH waves is assumed to be centered at $r = 0.05$ m and to have a Gaussian profile in radius with a width of 0.03 cm. For the LH heating power deposition and for the numerical implementation of the LH model see Ref. [55]. The heat source sustains the pressure profile against turbulent heat losses as well as helps in increasing slowly the ion temperature over 200 eV during the simulation time 150 μs (time step 5×10^{-8} s in an $N_r = 30$, $N_\chi = 200$, $N_\zeta = 4$ grid). The pressure profile appears to become stabilized at the balance between heating and heat losses after 100 μs simulation. Fig. 1 shows also the evolution of the radial electric field averaged over the steepest pressure gradient region compared asymptotically with the correspondingly averaged standard neoclassical estimate for E_r [51] evaluated from the shown density and temperature profiles with zero averaged parallel flow velocity (no significant parallel ion flow was developed during the simulation).

Both the potential and E_r are seen to evolve through GAM oscillations to a quasi-steady-state in quantitative agreement with the neoclassical estimate. A similar asymptotic behavior in agreement with the standard neoclassical estimate has been found also in other runs where either the pressure gradient was not too strong or plasma current was not too small and which covered a wide range of collisionalities ranging from collision dominated region to banana region. However, enhanced E_r at the region $M_\mathrm{p} \equiv E_r/v_{Ti}B_\mathrm{p} \sim 1$, and, in particular at outer radii, the contribution of Reynolds stress and viscosity of turbulence have been identified. Further study of these effects is given in Section 6 and in a separate publication [58].

Having the collisionality $\nu_{*i} = 4$ and $q_s = 3.58$ at $r = 0.05$ m in the present case of Fig. 1, the GAM oscillations are not strongly damped at this steep gradient region according to the analytical theory of GAM oscillations (see, e.g. [59]). This can also be observed in the figure as persistence of the oscillations. One should note that the relatively rapid changes in the pressure profile and neoclassical potential may also amplify the GAM oscillations. This explains partly the occasional pick up in the strength of the oscillations as seen in the figure.

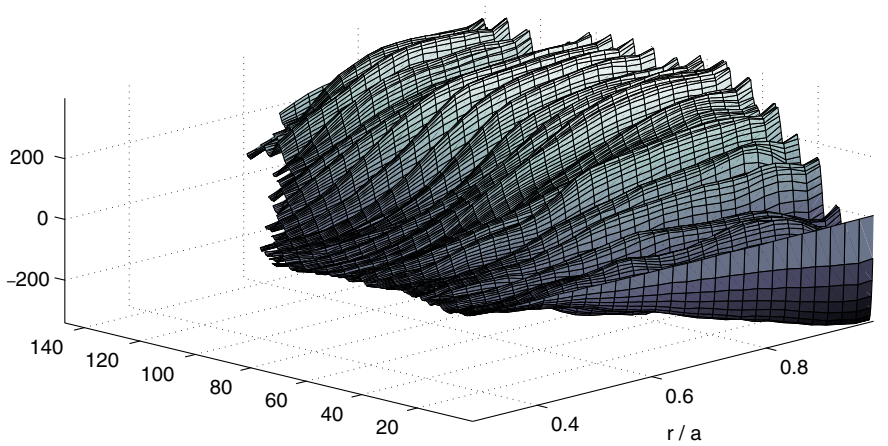

The analytical GAM period $\omega_{\mathrm{Gam}}^{-1} \approx 2.4$ μs at $r = 0.05$ m is somewhat longer than 1.6 μs found in Fig. 1. However, one should note that the global nature of the present simulations coupling different radial regions of different q_s and temperature together makes the present comparison difficult. In fact, as seen in Fig. 1, the GAM oscillations at different radii do not proceed in phase, and obviously strongly interact producing a complex evolution of the potential profile in time.

To make a more detailed comparison with the theory, collisionless simulations in a homogeneous plasma (with the same FT-2 configuration as in Table 2) with kinetic electrons and with a current density profile providing constant q_s over the simulated radial region were performed. In Fig. 2, both the angular frequency and

the residual level for the GAM oscillations seen in the simulations have been plotted against the analytical expressions $\omega_{\mathrm{Gam}} = (7/4 + T_e/T_i)^{1/2} v_{Ti}/R$ [59] and $A_R = 1/(1 + 1.6 q_s^2/\sqrt{r/R})$ [60] for the GAM oscillation frequency ω_{Gam} and the Rosenbluth residual level A_R. The resulting values have been produced at $r/a = 0.75$ for a variety of plasma ion and electron temperatures (90–360 eV), magnetic field (0.6–2.45 T), major radius ($R = 0.3 - 0.9$ m) and $q_s = 1.28$–2.91. The plasma density was 5.1×10^{19} m^{-3}. Even in the present case with constant q_s, the determination of the GAM characteristics is complicated through the effect of boundaries which in a relatively early stage after a few oscillation periods start affecting the GAM oscillation in the radial interior of the simulation region. In spite of this, a fair agreement with the theory for the GAM frequency and residual level is found. It should be noted that the GAM theory has been developed for adiabatic electrons, radially periodic boundary conditions, and for a flux surface averaged electrostatic potential only. To ease the comparison, part of the simulation runs were performed by flux surface averaging both the electrostatic potential and the charge separation in Eq. (2) before the guiding center calculations and inversion of Eq. (2), respectively. The GAM frequencies were found to agree with the theory equally well irrespective of this simplification. However, the agreement for the residual levels was obtained only in the presence of this flux surface averaging. In the presence of collisions, a similar agreement for frequencies was found but the residual level was damped away together with the oscillations. The collisionless damping was in general found to be stronger than Landau damping predicts. This is believed to arise from the presence of kinetic electrons (with adiabatic electrons, a closer agreement with the theory prediction of the Landau damping was obtained) and from the radial aperiodicity and finite orbit widths crossing the boundaries. It is the global nature of the present code which makes the GAM analysis thus a much more difficult task (but also more realistic) than for flux tube delta f simulations [16] where the field is made periodic in radial direction.

5.2. Linear growth of unstable modes

Whatever a nonlinear model is used in drift wave turbulence modelling, it should produce the same physics (growth rates γ and frequencies ω_r of unstable drift waves) in the linear regime as any other model. Although this is the most fundamental test to which every code must agree to a reasonable degree, it does not guarantee proper nonlinear behavior. With a full f code linear benchmarking is challenging, because of background variation for plasma densities, temperatures and charge separation, and of course – numerical noise.

Traditionally in delta f codes the linear analyses are performed using a local Maxwellian background distribution, which is simple to implement and produces adequate results. However, in the case of a full f code, creation of such a stable background is not trivial due to finite banana width effects which produce rather large oscillations in the ion density (and profiles). One solution is to adopt the quiescent start-up for the distribution described in the previous chapter. It has been observed with delta f calculations [17] that this kind of procedure produces some difference in the growth rates of unstable modes, tending to reduce growth rates slightly with respect to calculation with a local Maxwellian initialization. Linear analyses in the adiabatic electron case have been studied with both quiescent and local Maxwellian initialization, but the results given in Fig. 3(a) are produced with local Maxwellian ion initialization. In the kinetic case where the initialization plays a more important role, however, the quiescent initialization is used.

In both the adiabatic and kinetic linear cases, we perform the linear analyses in the code by selecting a specific toroidal mode number n in the field equation, while allowing the whole spectrum of corresponding poloidal mode numbers m. The quasi-ballooning coordinate system optimizes the mode spectrum so that only modes near the resonance criterion $|m\iota + n| \leqslant N_\zeta/2$, evaluated at the resonant surface $r = r_0$, are supported, where N_ζ is the total number of toroidal grid cells. When we pick only one toroidal mode number n as the target of simulation, we are effectively modelling also $q_s N_\zeta$ poloidal mode numbers. The n filtering is done to remove the effects of toroidal mode coupling and mode selection, especially important for off-maximum modes. The mode structure is then output from ELMFIRE data by Fourier analysis in the quasi-ballooning coordinate system [44], and the results are calculated from the energy associated with each mode near the resonant flux surface at r_0. The corresponding $k_\theta \rho_{\mathrm{i}}$ in Figs. 3(a) and (b) are obtained from the resonance criterion $m = -nq_s$ (which corresponds to the mode $k_\parallel = 0$) and we use $k_\theta = m/r$. The growth rates are tabulated for amplitudes of potential perturbations, not for the mode energy. It should be noted that in present simulations with $q_s N_\zeta$ poloidal modes growing at the same time, there is a coupling among these modes already at the lin-

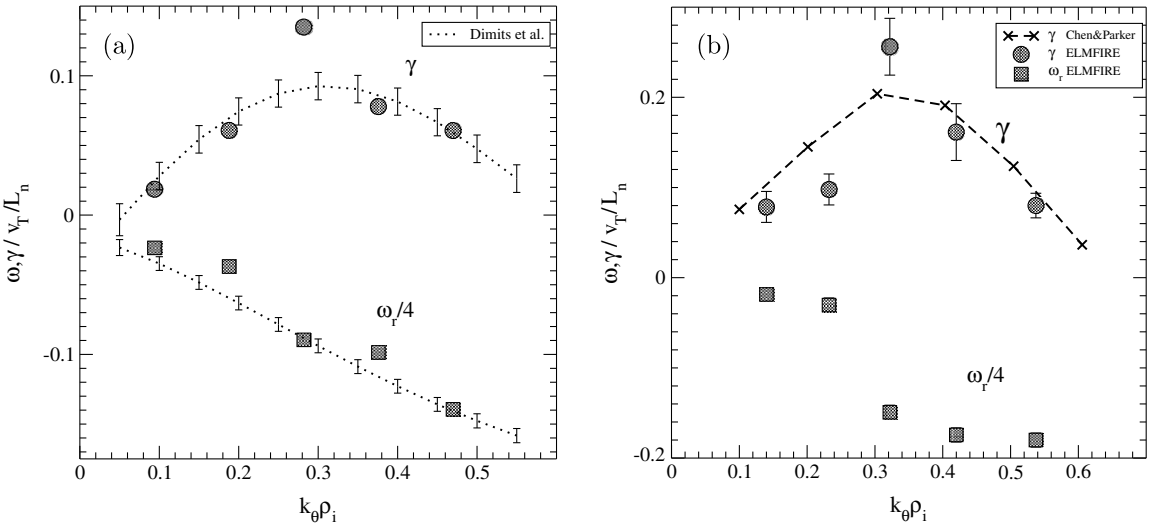

Fig. 3. Linear growth rates and frequencies for the "Cyclone base case" parameters with adiabatic (a) and kinetic (b) electrons as a function of $k_\theta\rho_i$ at $r/a = 0.5$. The ELMFIRE simulation results are compared to the delta f code results from Dimits et al. [13] and Chen and Parker [42].

ear stage. In fact, the different m modes are resonant at slightly different radii around r_0 and grow at slightly different rates making the determination of the growth rate (and frequency) somewhat arbitrary. It is not clear, whether the total energy of the mode n (including the energies of all m modes attached to it) or the energy of the resonant mode $m = -nq_s$ at r_0 only (as in the present work) has been used for the growth rate and frequency evaluation in benchmark tests of the other simulation codes.

In the linear regime, the ELMFIRE is tested in two different ways: we examine the linear growth of ion temperature gradient modes with the adiabatic electron model within the "Cyclone DIII-D base case" parameter set [61] (given in Table 1). The kinetic electron model presented in Section 3.2 is benchmarked adhering to the parameters given in Ref. [42], which has otherwise the same parameters as the adiabatic case but the electron profile is given by $T_{e0} = T_i(r_0)$, $L_{Te} = \infty$, and the electron–ion collision frequency in the linear stability analyses is given by $\nu_{ei}L_n/v_{Ti} = 0.14$ (whereas in the adiabatic case, no collisions were present). The results for the adiabatic electron case are shown in Fig. 3(a) which have a fair agreement with the results obtained with other gyrokinetic code results [13]. The main deviations, in particular in the growth rate, arise from the relatively high noise level the present full f calculation has with a reasonable number of simulation particles. Here, the time step 2×10^{-7} s in an $N_r = 30$, $N_\chi = 300$, $N_\zeta = 16$ grid was applied using 384 ions per grid cell.

In Fig. 3(b) we present the results on the kinetic electron simulation of the Cyclone base case. Because the electron temperature gradient is small, the main contribution should be from the ITG branch of the instability like in the adiabatic case. The present results should be compared to the results obtained in [42] where about 1.5–2 higher growth rates were obtained than in the adiabatic case. The present full f simulation results have a fair agreement with the growth rate values of the modes obtained from [42], in particular for $k_\theta\rho_i$ values at maximum growth and for larger values. Here, for the present kinetic simulation the time step 5×10^{-8} s in a grid of $N_r = 30$, $N_\chi = 300$, $N_\zeta = 16$ was applied using 256 ions per grid cell. Due to the electron motion, the noise level is enhanced and running average filtering of the data using a time window of 80–160 time steps was used to extract the frequencies and growth rates from the Fourier mode energies. At the low $k_\theta\rho_i$ range the agreement with the results obtained in [42] is poor. There are several reasons for this which all arise from the finite number of simulation particles that is feasible within the computational resources available for the present runs. First, due to the low angular frequency of the modes in this regime, the modes are locked to the growth relatively slowly. Secondly, as pronounced mode perturbations well above the average noise for certain m modes at the initialization are difficult to avoid in the full f simulation, the growth of any selected mode can

suffer from mode coupling to the modes at pronounced level at initialization. Thus, the error margins for the mode growth in the long wavelength limit are noticeable in our present runs. The angular frequency of the modes in [42] was presented only for $k_\theta \rho_i = 0.3$, and therefore these angular frequency values are not plotted in comparison with the present simulation results in Fig. 3(b). It is however noted that the value $\omega L_n / v_{Ti} \sim -0.54$ at $k_\theta \rho_i = 0.3$ from [42] supports the angular frequency values obtained from the present simulation.

5.3. Collisional nonlinear behavior

In saturation (nonlinear regime) of drift wave turbulence the only widely used benchmark is the study of level and scaling of ion heat diffusion constant χ_i as a function of R/L_T. There has been much emphasis on this benchmark over the simple linear stability analyses, which have been found not to always reflect the more complex nonlinear physics, as it was shown that some models produce significantly different scaling from the gyrokinetic particle models [13,61], even though they reproduce the same linear behavior.

In the saturation runs the parameters given in Table 1 and in the beginning of this Section were chosen except deuterium instead of hydrogen was selected for the ion species. The time step of 7×10^{-8} s in an $N_r = 30$, $N_\chi = 300$, $N_\zeta = 8$ grid with $N = 1500$ particles per cell was used. It is important to note, that in the nonlinear saturation case with kinetic electrons Chen et al. [42] used $\nu_{ei} L_n / v_{Ti} = 0.45$, which differs from that used in the linear growth analyses. In the kinetic case in Fig. 4 we set $\nu_{ei} L_n / v_{Ti} = 45$ and $n_0 = 4.5 \times 10^{19}$ m^{-3}, i.e., 100 times stronger collisionality than in Ref. [42].

With the parameters and data of the case in Fig. 4 for $N = 1500$ we obtain $D = 0.4$ m^2/s from Eq. (9). This should be compared to the value of $\chi \sim 0.5$ m^2/s obtained at initial stages of simulation. This level was found to scale as $1/N$ in the present case in the simulations.

Using the mixing-length estimate for the physical level of fluctuations, the radial ion heat conductivity can be estimated from $\chi = (5/2)(L_T/L_n)(v_{Ti}^2/\Omega_i)(1/k_\perp L_n)g$, where g arises from the relation $\delta n = ne\Phi(1 - ig)/T$ between the density and potential fluctuations. Using $g \sim \gamma/\omega \sim 0.5$ from the linear growth rate analysis for the collisionless Cyclone Base case in Fig. 4, we may estimate $\chi \sim 0.3$ m^2/s for the collisional case of Fig. 4. This is lower than what we predict and find for the ion heat conductivity by noise. This was further confirmed by running for saturation in the absence of collisions. Here, as shown in Fig. 4, χ does not evolve from its initial fluctuations and stays at a level of 0.5 m^2/s. Therefore, the ion heat conductivity arising in the collisional case of Fig. 4 must originate from the neoclassical ion heat conductivity. The heat conductivity by

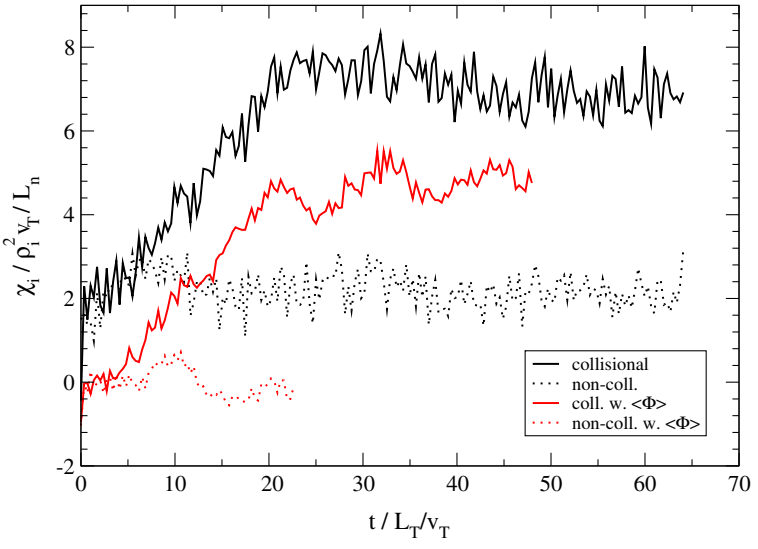

Fig. 4. The saturation of the ion heat diffusion constant χ_i for the Cyclone base case parameters with $R/L_T = 6.9$ at high collisionality in time, in simulation with kinetic electrons. Four cases are shown: flux-surface averaged and non-averaged, with collisions and without.

turbulence is not strong enough to be identified with the present parameters. Other runs made by flux-surface averaging the potential to remove the noise and turbulent heat flux confirm the neoclassical origin of the physical ion heat flux in Fig. 4, where the results of such runs are also shown with and without collisions. No initial heat flux is found with flux-surface averaged potential runs indicating the absence of the noise flux in such runs. Here, in the collisional case, $\chi \sim 1.3\ \mathrm{m}^2/\mathrm{s}$ at saturation is found. This is comparable to that obtained without flux-surface averaging, after the noise contribution as detected in the initial phase of the run is subtracted.

From Eq. (12), we calculate the analytical neoclassical ion heat conductivity of $1.2\ \mathrm{m}^2/\mathrm{s}$ for the present parameters, which is in fair agreement with the present simulation result. In the case of Fig. 4, the radial electric field was found to be negative and in good agreement with the neoclassical estimate, as the noise flux was smaller than the ion flux due to ion–ion collisions. On the other hand, in its collisionless run, the radial electric field was positive and was determined by the non-ambipolarity of the noise flux. The closer investigation of this effect is beyond the scope of the present paper and has been elaborated in more detail in [58].

5.4. Turbulent nonlinear behavior and numerical convergence

In Ref. [13] it was shown that in delta f codes χ_i may fail to saturate properly if the number of simulation particles is too small. In Fig. 5, the radial profile of (a) χ_i, (b) heat flux and (c) temperature profile at time 125 μs (time average over 5 μs) with different numbers of simulation particles using FT-2 parameters (deuterium plasma) is shown. Here, the convergence of χ_i as the number of simulation particles is increased can be clearly seen and 500 particles in a cell is shown to be enough for it. Also, in the simulation of GAM frequency discussed in Section 5.1 this was found to be sufficient amount of particles. Unlike in Ref. [13], our simulations show mainly an increase in the noise in χ_i when the number of test particles decreases while χ_i never fails to saturate. This gives confidence in the new full f implicit scheme.

One way to reduce noise is to decrease the number of grid points keeping the number of test particles constant thus increasing the number of particles in each cell. However, then we are not able to resolve all the interesting modes anymore. With the present parameters, in absence of turbulence, the initial transient following from an incomplete non-quiescent initialization was not found to be sensitive to the grid size. However, in the presence of turbulence, the initial phase was very different in the cases with grids of $31 \times 200 \times 4$ and $45 \times 300 \times 4$. Thus, the grid size seems to have an effect to the transient at least when electric field is left to influence the guiding center orbits of the ions.

Effect of grid size in poloidal direction to the saturation level is shown in Fig. 6. There, χ_i value at time $t = 175$ μs averaged over 10 μs is shown for grid size values $N_\chi = 50$, 100 and 200 with 200 particles in each cell using FT-2 parameters and kinetic electrons. Here, one can see that both $N_\chi = 100$ and 200 give very similar results. However, $N_\chi = 50$ fails to give the same result at the outer radii where the grid size $r\Delta\chi = 2\pi r/N_\chi$ is already of the order of 1 cm thus being unable to resolve modes. However, this is not a problem near the inner edge where $r\Delta\chi = 2$–3 mm and all results are close to each other. One measure of accuracy in gyrokinetic simulations is the ratio of grid size to the Larmor radius, $x_{\chi\rho} = r\Delta\chi/\rho_\mathrm{i}$, which at the inner radius ($r = 0.02$ m), at the mid radius ($r = 0.05$ m), and at the outer radius ($r = 0.08$ m), gives $x_{\chi\rho} = 2.7, 7.8$ and 22 for $N_\chi = 50$,

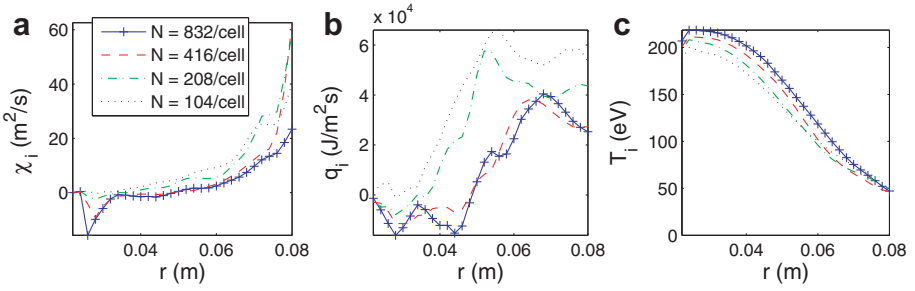

Fig. 5. Radial profile of (a) χ_i, (b) heat flux and (c) temperature profile at time 125 μs (time average over 5 μs) with different numbers of simulation particles. FT-2 parameters with kinetic electrons are used in this simulation.

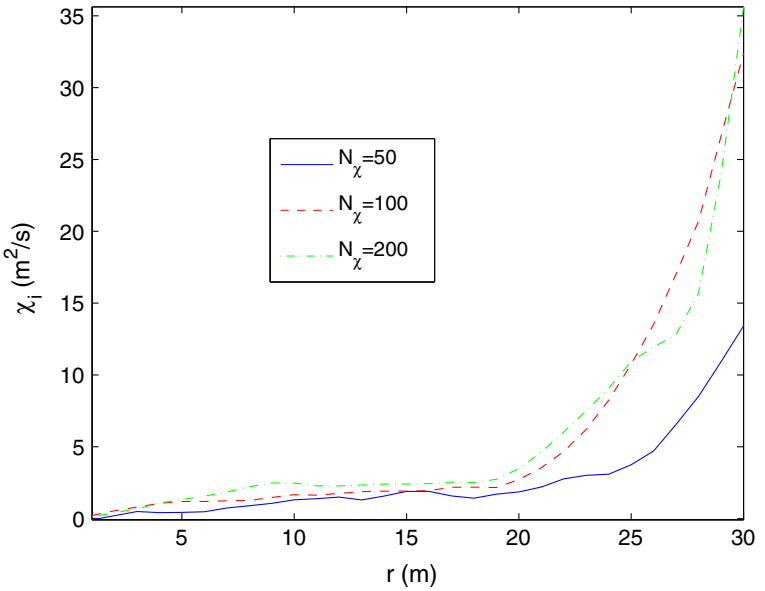

Fig. 6. Radial profile of χ_i at time 175 μs (time average over 10 μs) with different numbers of grid points in poloidal direction. FT-2 parameters with kinetic electrons are used in this simulation.

$x_{\chi\rho} = 1.4, 3.9$ and 11 for $N_\chi = 100$ and $x_{\chi\rho} = 0.68, 2.0$ and 5.4 for $N_\chi = 200$ in poloidal direction, respectively, for characteristic temperatures shown in Fig. 5c. Here ρ_i decreases (as T_i becomes smaller) same time as r increases making the ratio $x_{\chi\rho}$ increase strongly towards the outer edge. In radial direction Δr is typically constant and for the present case we get $\Delta r/\rho_i = 2.2, 2.5$ and 4.3.

In Fig. 4, the collisional case of Cyclone base parameters was considered where the ion heat conductivity is dominated by neoclassical transport mechanisms. To find the turbulent behavior, the Cyclone base case with $R/L_{Ti} = 9.5$ and with the scaled parameters $r_L = 0.189$ m, $r_R = 0.448$ m, $a = 0.625$ m, $R = 1.7$ m, $B = 1.9$ T, and $I_0 = 590$ kA was considered with $n_0 = 4.5 \times 10^{17}$ m^{-3} and $T_0 = 2$ keV. The gradient scale lengths were $L_n = 0.76$ m, $L_{Te} = 100$ m, and $L_{Ti} = 0.17$ m. Like in the case of Fig. 4, deuterium ions were used. Here, the collisionality and thus the neoclassical transport are very weak. At $r = r_0$, $\rho_i/a = 0.005$ in this case. Fig. 7 shows how the ion heat conductivity at $r = a/2$ ($q_s = 1.4$) saturates after some overshoot. The convergence at the apparent saturation in spite of high noise level in the initial phase is found already with 1200 particles per cell. Here, a grid of $N_r = 30$, $N_\chi = 200$, $N_\zeta = 4$ was applied. Interestingly, as suggested by the behavior at large number of particles (4780 particles per cell), the initial noise flux seems to be not additive to the physical heat flux at saturation, but rather appears to be replaced by the latter. This can be considered as a natural consequence of upward cascading of unstable mode energy at saturation.

Further insight into the saturation is provided by Fig. 8 where the χ_i values obtained in Fig. 7 are arranged as a function of R/L_{Ti} and time in due course of the simulation. The obtained χ_i evolution reflects the features familiar from other (delta f) code results in similar cases [62]. After the overshoot and some steepening of the T_i radial profile, χ_i and T_i profile relax towards the gyroBohm condition $\chi L_n/\rho_s^2 v_{Ti} \sim 1$ for ion heat conductivity. Here, $\rho_s^2 v_{Ti}/L_n \approx 4.5$ m^2/s at saturation at $r = a/2$ from the simulation results. One can compare this χ_i value at $R/L_{Ti} = 9$ with the value of $\chi L_n/\rho_s^2 v_{Ti} = 1.3$ obtained in another simulation (see Fig. 2 in [63]) in the Cyclone base case where global delta f simulations (with adiabatic electrons) were performed. The important role of the global simulation over the flux tube calculation was already stressed in the latter work.

It is remarked here that full f simulation of nonlinear turbulence saturation in an adiabatic limit of electrons is problematic. This arises from the overly restricting constraints for particle and heat convection set by the adiabatic condition of electron density [see, e.g. Eq. (10) or a corresponding model with $\langle n_i \rangle$ replaced by a fixed n_{e0} in Eq. (10)] which in the presence of radial heat conduction by gradients and turbulence can lead in the full f treatment to radially localized potential perturbations and to an unphysical shear of poloidal flows with a

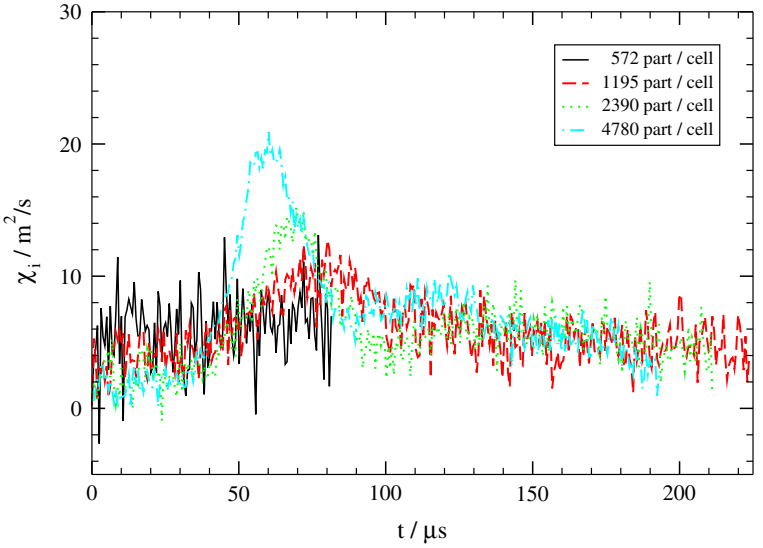

Fig. 7. χ_i at $r = a/2$ as a function of time with different number of simulation particles for the scaled Cyclone base case parameters with weak collisionality from simulation with kinetic electrons.

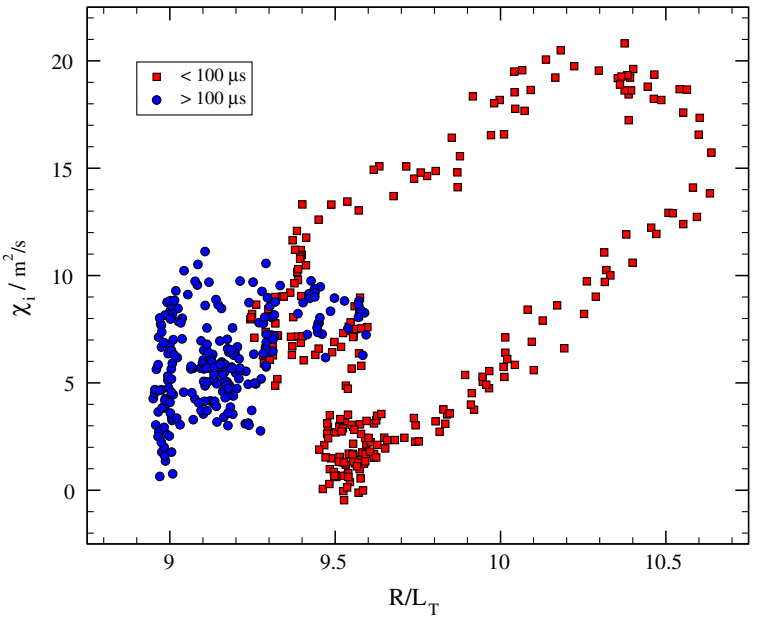

Fig. 8. χ_i at $r = a/2$ arranged as a function of time and R/L_{Ti} for the Cyclone base case in Fig. 7 using 4780 particles per cell.

concomitant decay of ion heat conductivity and no reasonable saturation of it. The study of this problem is beyond the scope of this paper and details of it will be presented in a separate publication.

It should also be noted that the simulated time in Fig. 7 is not long enough to conclusively regard χ_i as saturated in the present kinetic electron case. Also, the overshoot appears to still grow with the highest number of simulation particles. The latter observation can be understood on the basis of discussion at the end of Section 5.2. The increase of the number of simulation particles improves the quality of initialization and reduces the mode coupling with the noisy modes. Presently, the computing resources available for these runs do not allow a more detailed investigation of these issues within the full f formalism.

6. Global transport simulation of FT-2 tokamak plasmas

The developed code is here applied for global transport analysis in a plasma similar to FT-2 tokamak experimental plasma involving lower hybrid (LH) heating. In FT-2 tokamak [40], internal transport barrier has been observed with some 100 kW LH heating of ions. To model this experiment, simulations in a deuterium plasma with a minor radius of $a = 8$ cm, major radius of $R = 55$ cm, magnetic field $B = 2.2$ T, and plasma current of $I = 22$ kA have been conducted. At the outer edge, neutral particle ionization close to the limiter (with 1 cm radially inward decay length of the strength) provides the source of cold electron–ion pairs (at 0.1 eV) to replace the lost particles to the limiter. We have either started the simulation from the $T_e \sim 300$ eV, $T_i \sim 120$ eV, plasma just after the onset of the LH heating or from well heated ions with $T_i \sim 250$ eV. Grid parameters are $N_r = 31$, $N_\chi = 200$, $N_\zeta = 4$, and 11,520,000 ions are initialized in the calculation domain bounded by the radii $r_L = 0.02$ m, $r_R = 0.08$ m. The LH power deposition profile is taken off-axis, as in the case of Fig. 1 by adjusting the LH wave intensity profile in our LH heating model [55]. The density and temperature profiles are taken to be close to the experimentally measured ones at the simulation start. No impurities were considered, and the loop voltage was set at 0.5 V. In the experiment Oxygen impurities with plasma $Z_{\text{eff}} \sim 3$ are present and the loop voltage is around 3–4 V. The corresponding simulation results with experimental-like impurity content are discussed in [66].

For the case, where the initial conditions are close to that of observed internal transport barrier state (high ion temperature), the plasma potential (magnetic surface averaged) evolves as in Fig. 9, where rapid growth in the electrostatic potential is observed, well after the initial transients and turbulence saturation. In terms of poloidal Mach number $M_p \equiv E_r/v_{Ti}B_p$ the potential profile just before its rapid growth leads to $M_p \sim 1$ in the middle radii of the simulation region, thus warranting the consideration of the role of theory presented in Ref. [56] where a rotational runaway of E_r was observed when M_p approaches unity. The obtained inward radial electric field around $r = 0.04$–0.06 m well after the potential growth is about 2–4 times higher than the standard neoclassical prediction [51] (see Fig. 12).

Interestingly, after some 70 μs the radial electric field increases significantly in the middle of the plasma leading to a relatively strong shear in the $E_r \times B$ velocity at the radius $r \sim 6$ cm at $t \sim 110$ μs, which is found to stay there in longer runs. As seen in Figs. 10 and 11, this leads to a simultaneously appearing knee-point in the ion temperature profile at $r \sim 6$ cm and a rapid collapse of the heat and particle diffusion coefficients inside this radius. In Fig. 12, heat diffusivity χ_i, E_r, and the $\mathbf{E} \times \mathbf{B}$ flow shear are shown as a function of time at

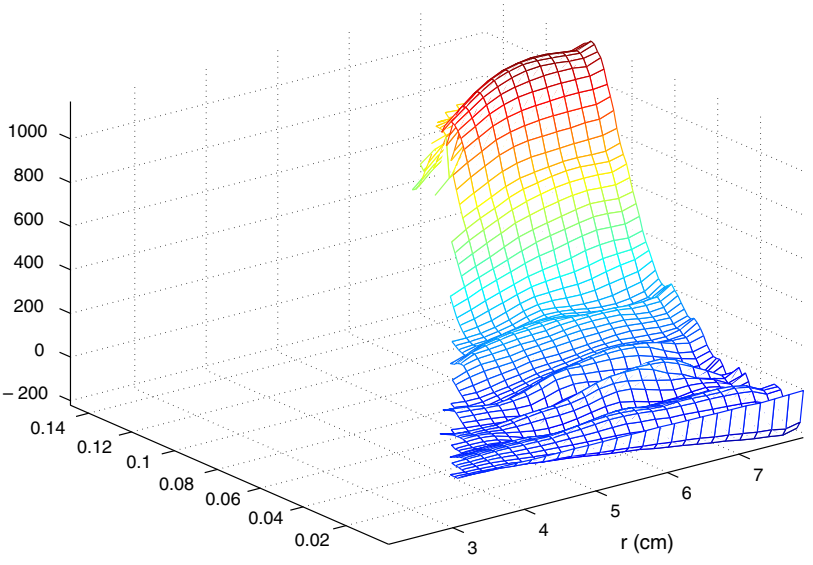

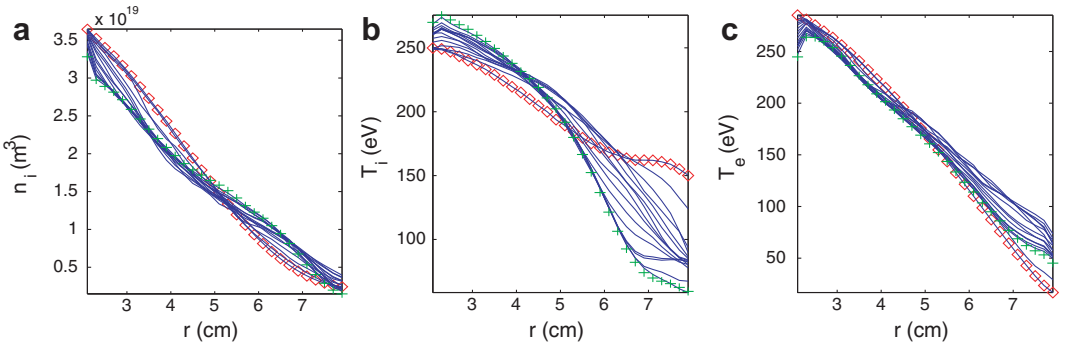

Fig. 10. Time traces of (a) ion density n_i, (b) ion temperature T_i and (c) electron temperature T_e before and after the rapid growth of the electrostatic potential. Here, diamonds denote the start and "+" the end of simulation.

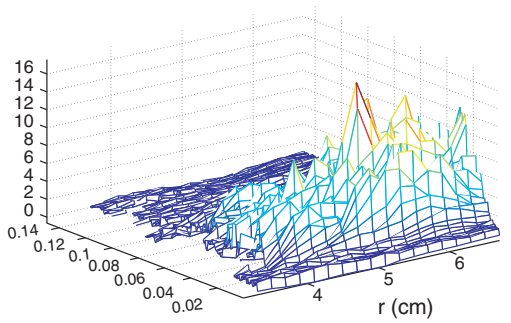

$r = 0.05$ m. Clear correlation between high shear and low χ_i is seen in the figure. The code diagnostics of turbulence shows contemporary suppression of broadband modes and related $\mathbf{E} \times \mathbf{B}$ convective cells together with the reduction of the size of the cells [64,65]. The ion heat diffusion coefficients 4–6 m^2/s and $< 1\ m^2/s$ before and after the transition, respectively, inside the position of the knee-point are close to those obtained in ASTRA interpretative modeling of the FT-2 discharge [40]. Also, the global energy confinement time as evaluated from the time rate of the plasma energy content, outflowing heat flux and heat sources (Ohmic heating and LH ion heating) was estimated to be close to the experimentally found value of 1 ms. In the present run, after the transition, the total energy of the plasma reaches an apparent steady-state, after some growth and decay. From the electron and ion radial fluxes at the outer radius r_R at steady-state one reads some 90–100 kW power outflowing from the system. This is compensated by 10 kW back flux by reinitialized 15 eV ion–electron pairs, 70 kW lower hybrid ion heating and 10 kW Ohmic heating in the plasma core, the rest being compensated by numerical electron heating.

The comparison of the simulated energy balance and confinement with the experiment can be here regarded as qualitative only, because many important elements of the energy balance have not been simulated or have not been taken into account accurately. For example, because of Oxygen impurity the loop voltage in the experiment was 3.5–4 V implying about 70 kW Ohmic power, i.e., significantly larger heating in Ohmic channel. Similarly, the LH power absorbed by ions based on ASTRA interpretative energy balance of the experiment was only about 20 kW, the rest of the 70–100 kW coupled LH power being deposited on electrons. Moreover, in the simulation the experimentally observed 30 kW impurity radiation loss was not modelled. Other less important energy loss channels like those in ionization and charge exchange were nor modeled in the present simulation. One should also note that the current density profile used in the calculation of the magnetic background was not fitted to the actual one in the experiment or to the one resulting from the adopted loop voltage profile (constant in radius) in the simulation, although the total plasma current

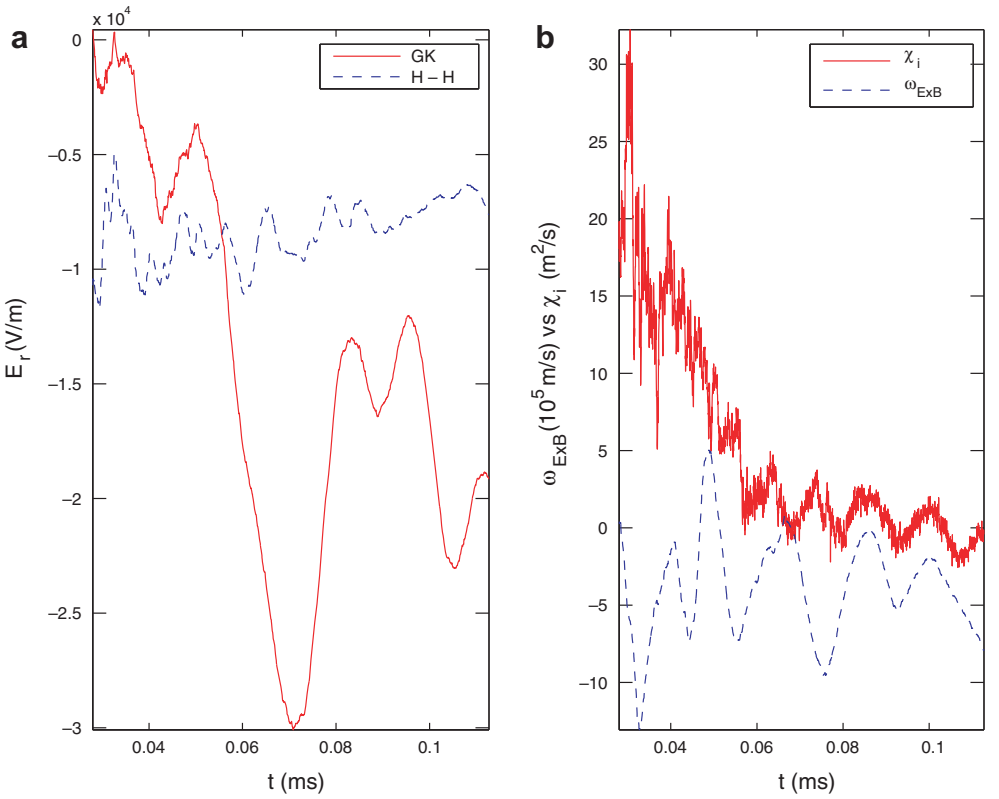

Fig. 12. (a) Flux surface averaged radial electric field at $r = 0.05$ m from the simulated potential profile and from the standard neoclassical estimate with simulated pressure profile as a function of time. (b) Heat diffusivity χ_i and $\mathbf{E} \times \mathbf{B}$ flow shear as a function of time at $r = 0.05$ m. Clear correlation between high shear and low χ_i is seen in the figure.

was the same in all cases. More detailed comparisons together with benchmarks against experimental diagnostics and characterization of the turbulence will be presented in separate works.

With hydrogen ions (hydrogen was used in experiments), similar abrupt onset of strong E_r enhancement and suppression of χ_i was not observed at the ion temperatures below 300 eV on axis, using otherwise the same parameters as in the deuterium case. However, at the high ion temperature range of the on-axis temperature around 250–300 eV stronger GAM oscillations in the potential and in the sheared poloidal flow were produced together with corresponding oscillations in χ_i. It is believed that the higher thermal velocity (at the same temperature) for hydrogen makes the $M_p \sim 1$ threshold higher for E_r. Also, the lighter mass of the hydrogen has been found to lead to larger χ_i than with deuterium. Therefore, obtaining the conditions for poloidal rotation speed-up neoclassically become more difficult to achieve for hydrogen. Further investigation of this needs a more careful consideration of the effect of impurities and boundary conditions on the ion pressure profile. This is beyond the scope of this paper and its study is deferred to future publications.

However, it is important to note that the plasma and transport evolution shown in Figs. 9–12 were confirmed in other ELMFIRE runs with variation of the grid size, number of simulation particles, and time step, and with different recycling conditions for the escaping particles, all neutrals recycled either at the outer boundary or deeper inside the plasma according to their ionization probability as described in Section 4.4. The impurities were not found to affect qualitatively the evolution of the profile of the electrostatic potential but some noticeable effects on radial transport coefficients were obtained [66]. The appearance of the knee-point at $r = 0.06$–0.065 m in the simulation was neither influenced by addition of charge-exchange process for the ions or the ionization energy loss for the electrons near the edge.

The growth of Φ over the standard neoclassical prediction at sufficiently high pressure gradient is also obtained (this takes place also with hydrogen) when flux surface averaged samples of ion and electron densities

are used in the GK equation of Φ, i.e., when the turbulence is suppressed. This implies that the potential difference seen in Fig. 9 arises from neoclassical effects. This particularly strong poloidal $\mathbf{E} \times \mathbf{B}$ flow for low current tokamaks was studied in detail in Ref. [55] with the earlier neoclassical version of ELMFIRE [2]. In agreement with it, at high plasma current $I > 35$ kA the present ELMFIRE version with the GK turbulence model produces a potential profile which follows the standard neoclassical prediction with no strong growth of it, at least up to $T_i(0) = 300$ eV. Here, no transport reduction is observed at $I > 35$ kA in agreement with experimental observations in FT-2. As already demonstrated in Fig. 1, the present ELMFIRE gives also the standard neoclassical prediction when the ion temperature on axis stays well below 250 eV, in agreement with the neoclassical simulations in [55].

7. Discussion

A first direct implicit ion polarization gyrokinetic full f particle-in-cell code has been written and is implemented with kinetic electrons in global tokamak transport simulations. The code is applicable for calculations of rapid transients and steep gradients in the plasma and is thus amenable, e.g. for studies of transport barrier formation. The particle advancing involves the polarization drift in line with the asymptotic theory in [36]. This is made possible by recording the charge density change due to the ion polarization drift at each time step. The use of Eq. (2) instead of standard gyrokinetic Poisson equation to solve the potential relaxes the numerical problems in sampling $\langle f \rangle$ and its derivatives in constructing the coefficient matrix for this equation. The difference-like treatment of the ion polarization keeps the potential equation fully implicit, and thus the full f method can be applied in an straightforward manner. Although making the code more memory and CPU time consuming than with the standard integrated GK polarization model, an efficient simulation of the full particle distributions for quasineutrality has been achieved.

Another important feature of the present full f code is the fully implicit treatment of the electron parallel nonlinearity. Stable performance with the whole drift-kinetic electron distribution with no significant numerical heating has been obtained with time steps set somewhat smaller than set by the Courant condition of the grid for the free streaming of electrons. Charge density responses in the gyrokinetic Poisson equation to both the electron parallel nonlinearity and ion polarization drift are constructed directly and implicitly from the particle coordinates during their advancement. This increases the statistical noise in the present particle full f method as does also the consideration of the whole particle distribution in comparison to delta f method.

Numerical noise due to particle discreteness and its contribution to the transport fluxes and neoclassical equilibrium have been found to be a subtle matter for full f particle simulations. The careful study in both collisional and turbulent limit of transport has helped to separate and identify the contribution of noise, and scaling rules for ensuring sufficient number of simulation particles for noise suppression have been found.

The present code has been validated against the linear predictions of the unstable mode growth rates and frequencies both in adiabatic and electron kinetic Cyclone Base case. For electron kinetic calculations, the goodness of the initialization is found to be important for the identification of the mode growths under the noise. In the electron kinetic case, the evolution of the ion heat conductivity is found in agreement with the neoclassical estimates at high collisionality. At weak collisionality, the heat conductivity by turbulence has been studied. However, here the benchmarking with other electron kinetic codes is still ongoing. A first validation of the neoclassical radial electric field in the presence of turbulence for a heated collisional tokamak plasma is obtained. The agreement with the standard neoclassical prediction [51] is found for plasma pressure gradients having $M_p \ll 1$ (see also [58]), but with steep ion temperature profiles making $M_p \sim 1$ according to standard neoclassical prediction (i.e., the ion orbit width becomes of the order of the gradient scale length), a significant enhancement of the radial electric field over the standard neoclassical prediction is observed. This enhancement appears to arise from the so called rotation runaway effect predicted in [56] as indicated by the work [67].

The neoclassical radial electric field together with the related GAM oscillations has been found to regulate the turbulence and heat and particle diffusion levels in a large aspect ratio tokamak at low plasma current. The simulations have been particularly encouraging, as many characteristics of neoclassical theory have been reproduced, even in the presence of turbulence at appropriate limits, including the magnitude of radial electric field, ion heat conductivity, and parallel conductivity (not discussed in the present work). The level of turbu-

lent transport has been of the right order of magnitude in comparison to experimental measurements at FT-2, although no characterization of the turbulence and comparison with experimental diagnostics has yet been finished. Clear indication is found for turbulence to experience suppression at low plasma current and at sufficiently strong ion heating in much the same way as in experiments. Kolmogorov-type power laws $S(k) \propto k^{-\alpha}$ with radially dependent $\alpha = 1 - 3$ have been obtained from the simulated fluctuations [65]. Here, the spectral behavior and cross-correlation studies of fluctuations from ELMFIRE through the growth of ion temperature in FT-2 discharges support the picture of long wavelength turbulence suppression at the increase of the shear in the poloidal flow.

Any direct comparison of the simulated radial electric field with the FT-2 experiments for the transport barrier conditions has been hampered by the absence of an appropriate measurement system of the poloidal flow velocity at FT-2 in the high plasma density and temperature range. A detailed comparison of the Doppler reflectometry data from FT-2 plasma fluctuations in Ohmic discharges with the corresponding ELMFIRE simulation data is in progress. It is expected that the present simulations of the poloidal flow and turbulence characteristics for the FT-2 can be compared in near future with direct measurements of these quantities using Doppler reflectometry and enhanced microwave scattering techniques.

The developed full f code can be presently used for electrostatic drift wave like transport simulations together with the neoclassical mechanisms in tokamak plasmas, but a number of problems related to boundary effects, all of them not discussed in the present work, and inclusion of the EM field with magnetic flutter, realistic magnetic configuration with non-circular non-concentric magnetic surfaces, and sheath effects close to material surfaces have still to be resolved. Moreover, the present full f approach is CPU time and memory consuming and its realization for large tokamaks cannot yet be considered due to the large number of particles required for a reasonable statistics. Recently, several initiatives for developing 5D global full f gyrokinetic Vlasov continuum codes for the toroidal plasma simulation have been launched [23,26,68] with a motivation of avoiding the numerical noise inherent, in particular, in edge plasma particle simulations. Together with the gyrokinetic continuum codes and other full f particle codes under development, the present full f gyrokinetic particle approach can be cross-validated in future and these tools may prove to be valuable, in particular, for the challenging tokamak scrape-off layer and pedestal plasma physics studies.

Acknowledgments

The computing facilities of CSC – Scientific Computing Ltd. were used for this work. We especially thank all the members of the IMP#4 project and its leader B. Scott of the Integrated Tokamak Modelling Task Force for their help and input. This research is supported by the Tekes Grant No. 40481/05. The co-operation with the FT-2 facility at the Ioffe Institute, St. Petersburg was supported by the Academy of Finland and EU INTAS Grant No. 05-1000008-8046. The authors are also grateful to E. Gusakov, S. Lashkul, and L. Villard for discussions, and R.R.E. Salomaa for his continuing support.

References

[1] J.A. Heikkinen, T.P. Kiviniemi, A. Peeters, Neoclassical radial current balance in tokamaks and transition to the H mode, Phys. Rev. Lett. 84 (2000) 487.
[2] J.A. Heikkinen, T.P. Kiviniemi, T. Kurki-Suonio, A.G. Peeters, S.K. Sipilä, Particle simulation of neoclassical plasmas, J. Comput. Phys. 173 (2001) 527.
[3] C.S. Chang, S. Kue, H. Weitzner, Numerical study of neoclassical plasma pedestal in a tokamak geometry, Phys, Plasmas 11 (2004) 2649.
[4] C.Z. Cheng, H. Okuda, Numerical simulation of trapped-electron instabilities in toroidal geometry, Phys. Rev. Lett. 41 (1978) 1116.
[5] R.D. Sydora, J.N. Leboeuf, D.R. Thayer, P.H. Diamond, T. Tajima, Three-dimensional particle simulation of drift-wave fluctuations in a sheared magnetic field, Phys. Rev. Lett. 57 (1986) .326.
[6] M.J. LeBrun, T. Tajima, M.G. Gray, G. Furnish, W. Horton, Toroidal effects on drift wave turbulence, Phys. Fluids B5 (1993) 752.
[7] W.W. Lee, Gyrokinetic approach in particle simulation, Phys. Fluids 26 (1983) 556.
[8] A.J. Brizard, T.S. Hahm, Foundations of nonlinear gyrokinetic theory, Rev. Mod. Phys. 79 (2007) 421;
D.H.E. Dubin, J.A. Krommes, C. Oberman, W.W. Lee, Nonlinear gyrokinetic equations, Phys. Fluids 26 (1983) 3524.
[9] H. Qin, R.H. Cohen, W.M. Nevins, X.Q. Xu, General gyrokinetic equations for edge plasmas, Contrib. Plasma Phys. 46 (2006) 473.

[10] P.J. Catto, A. Simakov, A new, explicitly collisional contribution to the gyroviscosity and the radial electric field in a collisional tokamak, Phys. Plasmas 12 (2005) 114503.
[11] R.D. Sydora, Three-dimensional gyrokinetic particle simulation of low-frequency drift-wave turbulence, Phys. Fluids B2 (1989) 1455.
[12] S.E. Parker, W.W. Lee, A fully nonlinear characteristic method for gyrokinetic simulation, Phys. Fluids B5 (1993) 77;
A.M. Dimits, Ph.D thesis, Princeton University, 1988.
[13] A.M. Dimits, G. Bateman, M.A. Beer, et al., Comparisons and physics basis of tokamak transport models and turbulence simulations, Phys. Plasmas 7 (2000) 969.
[14] Y. Chen, S. Parker, Gyrokinetic turbulence simulations with kinetic electrons, Phys. Plasmas 8 (2001) 2095.
[15] F. Jenko, W. Dorland, Nonlinear electromagnetic gyrokinetic simulations of tokamak plasmas, Plasma Phys. Control. Fusion 43 (2001) A141.
[16] J. Candy, R.E. Waltz, An Eulerian gyrokinetic-Maxwell solver, J. Comput. Phys. 186 (2003) 545.
[17] Y. Idomura, S. Tokuda, Y. Kishimoto, Global gyrokinetic simulation of ion temperature gradient driven turbulence in plasmas using a canonical Maxwellian distribution, Nucl. Fusion 43 (2003) 234.
[18] C.C. Kim, S.E. Parker, Massively parallel three-dimensional toroidal gyrokinetic flux-tube turbulence simulation, J. Comput. Phys. 161 (2000) 589.
[19] Z. Lin, W.W. Lee, Method for solving the gyrokinetic Poisson equation in general geometry, Phys. Rev. E 52 (1995) 5646.
[20] R.D. Sydora, Toroidal gyrokinetic particle simulations of core fluctuations and transport, Phys. Scr. 52 (1995) 474.
[21] L. Villard, S.J. Allfrey, A. Bottino, et al., Full radius linear and nonlinear gyrokinetic simulations for tokamaks and stellarators: zonal flows, applied $E \times B$ flows, trapped electrons and finite beta, Nucl. Fusion 44 (2004) 172.
[22] G. Furnish, W. Horton, Y. Kishimoto, M. LeBrun, T. Tajima, Global gyrokinetic simulation of tokamak transport, Phys. Plasmas 6 (1999) 1227.
[23] M. Brunetti, V. Grandgirard, O. Sauter, J. Vaclavik, L. Villard, A semi-Lagrangian code for nonlinear global simulations of electrostatic drift-kinetic ITG modes, Comput. Phys. Commun. 163 (2004) 1.
[24] C.S. Chang, S. Ku, M. Adams et al., Integrated particle simulation of neoclassical and turbulence physics in the tokamak pedestal/edge region using XGC, in: 21st IAEA Fusion Energy Conference, Chengdu, China, 2006, paper TH/P6-14.
[25] X.Q. Xu, Z. Xiong, M.R. Dorr, Edge gyrokinetic theory and continuum simulations, Nucl. Fusion 47 (2007) 809.
[26] Y. Idomura, M. Ida, S. Tokuda, Gyrokinetic toroidal full-f 5D Vlasov code GT5D, in: 34th EPS Conference on Plasma Physics, Warsaw, Poland, 2007, paper P-4.040.
[27] J.C. Cummings, PhD thesis, Plasma Physics Lab, Princeton University, 1994.
[28] B. Cohen, A. Dimits, J. Stimson et al., Implicit-moment partially linearized particle simulation of kinetic plasma phenomena, LLNL Report UCRL-JC-121734, September 1995.
[29] I. Manuilskiy, W.W. Lee, The split-weight particle simulation scheme for plasmas, Phys. Plasmas 7 (2000) 1381.
[30] Z. Lin, Global gyrokinetic particle simulations with kinetic electrons, Plasma Phys. Control. Phys. 49 (2007) B163.
[31] B.I. Cohen, T.J. Williams, Implementation of a semi-implicit orbit-averaged gyrokinetic particle code, J. Comput. Phys. 107 (1993) 282.
[32] W. Dorland, F. Jenko, M. Kotschenreuther, B.N. Rogers, Electron temperature gradient turbulence, Phys. Rev. Lett. 85 (2000) 5579.
[33] G. Manfredi, M. Shoucri, R.O. Dendy, A. Ghizzo, P. Bertrand, Vlasov gyrokinetic simulations of ion-temperature-gradient driven instabilities, Phys. Plasmas 3 (1996) 202.
[34] M. Shoucri, G. Manfredi, P. Bertrand, et al., Charge-separation velocity shear and suppression of turbulence at a plasma edge in the gyrokinetic approximation, J. Plasma Phys. 61 (1999) 191;
G. Manfredi, M. Shoucri, P. Bertrand, et al., Charge separation and velocity shear at a plasma edge in the finite gyro-radius guiding-center approximation, Phys. Scr. 58 (1998) 159.
[35] V. Naulin, Turbulent transport by higher-order particle drifts, Europhys. Lett. 43 (1998) 533.
[36] P.P. Sosenko, P. Bertrand, V.K. Decyk, Krylov–Boholiubov methods and gyrokinetics, Phys. Scr. 64 (2001) 264.
[37] A.B. Langdon, B.J. Cohen, A. Friedman, Direct implicit large time step particle simulation of plasmas, J. Comput. Phys. 51 (1983) 107.
[38] S.I. Lashkul, V.N. Budnikov, E.O. Vekshina, et al., Effect of the radial electric field on lower hybrid plasma heating in the FT-2 tokamak, Plasma Phys. Rep. 27 (2001) 1001.
[39] A.I. Morozov, L.S. Soloviev, Reviews of Plasma Physics, vol.2, Consultants Bureau, New York, 1968, p. 201;
R.B. White, Canonical Hamiltonian guiding center variables, Phys. Fluids B2 (1990) 845.
[40] M. Heikkinen, Krylov–Bogoliubov methods and gyrokinetics in an inhomogeneous plasma, Helsinki University of Technology Report, Espoo, 2007 (unpublished).
[41] J.A. Heikkinen, J.S. Janhunen, T.P. Kiviniemi, P. Kåll, Full f particle simulation method for solution of transient edge phenomena, Contrib. Plasma Phys. 44 (2004) 13.
[42] Y. Chen, S.E. Parker, B.I. Cohen, et al., Simulations of turbulent transport with kinetic electrons and electromagnetic effects, Nucl. Fusion 43 (2003) 1121.
[43] T. Takizuka, H. Abe, A binary collision model for plasma simulation with a particle code, J. Comput. Phys. 25 (1977) 205;
S. Ma, R.D. Sydora, J.M. Dawson, Binary collision model in gyrokinetic simulation of plasmas, Comput. Phys. Commun. 77 (1993) 190.
[44] A.M. Dimits, Fluid simulations of tokamak turbulence in quasiballooning coordinates, Phys. Rev. E. 48 (1993) 4070.
[45] R.B. White, M.S. Chance, Hamiltonian guiding-center drift orbit calculation for plasmas of arbitrary cross-section, Phys. Fluids 27 (1994) 2455.

[46] J.M. Dawson, Particle simulation of plasmas, Rev. Mod. Phys. 55 (1983) 403.
[47] L.M. Hively, G.H. Miley, J.A. Rome, Fast-ion thermalization in non-circular tokamaks with large-banana-width effects, Nucl. Fusion 21 (1981) 1431.
[48] W.W. Lee, Gyrokinetic particle simulation model, J. Comput. Phys. 72 (1987) 243.
[49] T.E. Stringer, Neoclassical transport in the presence of fluctuations, Nucl. Fusion 8 (1992) 1421.
[50] F. Ogando, A. Signell, J.A. Heikkinen, et al., Performance enhancements to ELMFIRE gyrokinetic code leading to new ranges of applications, ECA 30I (2006) P–4.15.
[51] F.L. Hinton, R.D. Hazeltine, Theory of plasma transport in toroidal confinement systems, Rev. Mod. Phys. 48 (1976) 239.
[52] C.S. Chang, F.L. Hinton, Effect of finite aspect ratio on the neoclassical ion thermal conductivity in the banana regime, Phys. Fluids 25 (1982) 1493.
[53] T.P. Kiviniemi, J.A. Heikkinen, A.G. Peeters, Test particle simulation of nonambipolar ion diffusion in tokamaks, Nucl. Fusion 40 (2000) 1587;
T.P. Kiviniemi, J.A. Heikkinen, A.G. Peeters, Effect of poloidal density variation on parallel viscosity for large Mach numbers, Phys. Plasmas 7 (2000) 5255.
[54] T.P. Kiviniemi, J.A. Heikkinen, A.G. Peeters, Neoclassical radial electric field and ion heat flux in the presence of the transport barrier, Contrib. Plasma Phys. 42 (2002) 236.
[55] T. Kurki-Suonio, S.I. Lashkul, J.A. Heikkinen, Formation and detection of internal transport barriers in low-current tokamaks, Plasma Phys. Controll. Fusion 44 (2002) 301.
[56] V. Rozhansky, M. Tendler, The effect of the radial electric field on the L–H transition in tokamaks, Phys. Fluids B4 (1992) 1877.
[57] S.V. Novakovskii, C.S. Liu, R.Z. Sagdeev, M.N. Rosenbluth, The radial electric field dynamics in the neoclassical plasmas, Phys. Plasmas 4 (1997) 4272.
[58] F. Ogando, J.A. Heikkinen, S.J. Janhunen, et al., Gyrokinetic full f modelling of plasma turbulence in tokamaks, paper TH/P2-13, in: IAEA Fusion Energy Conference, Chengdu, 16-21 October 2006, 21st Conference Proceedings, IAEA-CN-149;
S.J. Janhunen, F. Ogando, J.A. Heikkinen, et al., Collisional dynamics of E_r in turbulent plasmas in toroidal geometry, Nucl. Fusion 47 (2007) 875.
[59] V.B. Lebedev, P.N. Yushmanov, P.H. Diamond, S.V. Novakovskii, A.I. Smolyakov, Plateau regime dynamics of the relaxation of poloidal rotation in tokamak plasmas, Phys. Plasmas 3 (1996) 3023.
[60] M.N. Rosenbluth, F. L Hinton, Poloidal flow driven by ion-temperature-gradient turbulence in tokamaks, Phys. Rev. Lett. 80 (1998) 724.
[61] S.E. Parker, W. Dorland, R. Santoro, et al., Comparisons of gyrofluid and gyrokinetic simulations, Phys. Plasmas 1 (1994) 1461.
[62] S. Jolliet, A. Bottino, P. Angelino, et al., Ion and electron dynamics in nonlinear PIC simulations, AIP Conference Proc. 871 (2006) 124.
[63] S.E. Parker, C. Kim, Y. Chen, Large-scale gyrokinetic turbulence simulations: effects of profile variation, Phys. Plasmas 6 (1999) 1709.
[64] T.H. Ekholm, S. Janhunen, J.A. Heikkinen, S.V. Henriksson, T.P. Kiviniemi, Characteristics of transport barrier generation from gyrokinetic plasma simulation in a tokamak, IEEE Trans. Plasma Sci. 33 (2005) 442.
[65] S.V. Henriksson, S.J. Janhunen, T.P. Kiviniemi, J.A. Heikkinen, Global spectral investigation of plasma turbulence in gyrokinetic simulations, Phys. Plasmas 13 (2006) 072303.
[66] T.P. Kiviniemi, J.A. Heikkinen, S. Janhunen, S.V. Henriksson, Full f gyrokinetic simulation of FT-2 tokamak plasma, Plasma Phys. Controll. Fusion 48 (2006) A327.
[67] T. Kurki-Suonio, J.A. Heikkinen, S. Lashkul, Guiding-center simulations of non-local and negative inertia effects on rotation in a tokamak, Phys. Plasmas 14 (2007) 072510.
[68] X.Q. Xu, K. Bodi, J. Candy, et al., Continuum edge gyrokinetic theory and simulations, paper TH/P6-23, in: IAEA Fusion Energy Conference, Chengdu, 16-21 October 2006, 21st Conference Proceedings, IAEA-CN-149.